# Order in the domain structure in soft-magnetic thin-film elements: A review

by Hugo A. M. van den Berg

**The domain structure and its development in thin plane-parallel soft-magnetic elements have been investigated from both the experimental and the theoretical point of view. The experimental observations for verifying the predictions have been realized by means of the Bitter, Kerr, and Lorentz techniques.**

**In the first part, a self-consistent domain theory, based on micromagnetic principles, is unfolded for two-dimensional solenoidal magnetization distributions present in ideally soft-magnetic thin-film objects that are rectangular cylinders. The solenoidality implies that both the external field and the conduction currents are taken as zero. Two types of domain structures are distinguished: the basic structures in simply connected regions and the parallel configurations in special types of multiply connected regions—the parallel regions. A decomposition of the area of the object into disjunct subregions, either simply connected or of the parallel type, whose union completely covers the object, is put forward. A procedure for constructing all feasible parallel regions is presented. In each region, the appropriate solenoidal magnetization distribution is specified with which the magnetization M is taken parallel to the boundaries of the subregion. Thus, all the domain structures possible in the thin-film objects with arbitrary lateral shapes can be constructed. A number of experimental examples are provided.**

**In the second part, the M distribution is studied on a local scale, at which the requirement of solenoidality is dropped; i.e., external fields and conduction currents are allowed. The concept of the domain-wall cluster is introduced in order to obtain the maximum information about the M configuration in the entire object. Here, we employ the fact that domain walls are the preeminently visible features and that most information is available at those locations where a number of these**

**walls meet. A domain-wall cluster is the collection of all domain walls that have one region—the so-called cluster knot—in common. Three different categories of clusters characterized by the positions of their cluster knots with respect to the edges of the thin-film object are distinguished. Wall clusters with cluster knots at two, one, and no edges are defined as the corner, edge, and free clusters, respectively. General features of the magnetization distribution near the cluster knots are discussed for each of the above classes. The reversible transformations of the clusters are reviewed. Two different types of these conversions are recognized, to wit the cluster creation (fading) and the cluster furcation (fusion). Experimental evidence of these relationships is provided.**

**In the third part, the domain structures are considered as a concatenation of domain-wall clusters. During the domain-structure transformations, clusters are added to and removed from the domain-wall network. The conversions are reversible along specific branches of the hysteresis curves at which the changes can be comprehended in terms of the above reversible cluster conversions. Notwithstanding the reversible character at these branches, the domain configuration often develops itself into a subminimum of the energy, from which sudden irreversible transformations take place toward other branches with lower energy. In many cases, the latter alterations are attended by jumpwise adaptations in the overall object magnetization component along the field, and reveal themselves in the hysteresis curve. The part of the internal domain-wall structure in the hysteresis is elucidated, and its dependence on the film thickness is emphasized. Many examples are given for the purpose of demonstrating the strongly interwoven character of the domain network, the prehistory in the magnetic sense, the internal structure of the domain walls, and the macroscopic object hysteresis.**

## 1. Introduction

Since their origin, applications of ferromagnetic media have been hindered by the phenomena of magnetic domain structures which are inevitably associated with ferromagnetic materials. Nowadays, the situation is even more pressing, since devices with magnetic elements with dimensions in the (sub)micrometer range have become of great interest—particularly soft-magnetic elements such as thin-film heads [1, 2], magnetoresistive detectors [3, 4], cross-tie memories [5], and field-access bubble propagation circuits [6]—and such applications are greatly hampered by unpredictability in the magnetic domain configurations.

Various techniques have been used to circumvent the formation of domains, by almost complete suppression by an adequate lamination [7] of the soft-magnetic films and/or by biasing the **M** distribution (**M** = magnetization) with an appropriate effective field, so that a well-defined continuous **M**-state occurs in the film region that is critical to the device operation. This effective field may be induced by an electric current through a conducting shunt layer [8, 9], or by a permanent magnetic [10] or an antiferromagnetic shunt layer [11]. Although a significant improvement has been realized by film lamination, the domain effects still surface [12], partly because of the mismatch in the thickness between the various layers [13] and partly because of the magnetic history of the sample. Therefore, questions concerning the origin of the domain structure, its uniqueness, and its entanglement with the phenomenon of hysteresis have not lost any topicality, and such questions constitute the subjects of this paper.

We initially consider the issues of the inevitability of and the uniqueness in the domain structure in the ideally soft-magnetic plane-parallel thin-film elements. Until recently, the domain theory was still in the stage so aptly summarized by Brown [14]: "a patchwork of plausible assumptions, inspired by experimental observation, whose starting points are sometimes mutually inconsistent and cyclical." Pioneers in the domain theory, to wit Landau and Lifshitz [15] and Kittel [16], developed the following line of thought. The existence of domains, i.e., regions where the configurations bear a continuous character, and of domain walls, which are surfaces of jumpwise-rotating **M**, was accepted as experimental fact. The disintegration into domains was explained in terms of a trade-off of magnetic anisotropy and domain-wall and magnetostatic energy. In the bulk of the object, **M** was assumed to be parallel to one of the easy-anisotropy axes; however, continuation of this parallelism toward the bounding surface of the object led to magnetic surface charge, and hence to a high level of magnetostatic energy. To stave off the generation of magnetic charge, the domain walls were introduced, so that **M** was guided parallel to the boundary of the object, and a divergence-free coupling with **M** in the bulk, still supposed to be parallel to the easy axes, was achieved. Subsequently, the general features of the domain geometry were posited by taking a preliminary look at experimental data while a few geometrical parameters were left undetermined, in order to be able to

minimize the total energy. The lowest-energy configuration among a number of known domain geometries in a specific object was thus determined [17–19].

It is tempting to try to play the same tune: However, one must bear in mind that there is no self-consistent framework by which the above questions of domain inevitability and uniqueness can be treated. Moreover, the assumption of uniformity of **M** in the domains is premature in the soft-magnetic media with small intrinsic anisotropy. The micromagnetic theory [20] should constitute the basis for a self-consistent domain theory. Brown [14] claimed that a rigorous micromagnetic treatment should lead to domain-like and domain-wall-like regions. However, straightforward calculations lead to a system of nonlinear partial differential equations for the equilibrium distributions, and the demonstration of their stability has so far proved insuperable for arbitrary specimens. The present author does not attempt to cope with this general problem. Instead, he confines himself to a specific class of ideally soft-magnetic materials, to plane-parallel thin-film objects with cylindrical edges perpendicular to the film plane, and to objects that are not subjected to external field sources. It should be emphasized that in this section this implies that the intrinsic anisotropy of the medium is 0. Subsequently we discuss the impact of the intrinsic anisotropy; however, we will always confine ourselves to media with low $Q$ [$Q = 2K/(\mu_0 M_s^2)$], where $K$ is the anisotropy energy density and $M_s$ the saturation magnetization. Within these constraints, a self-consistent theory is elaborated by which definite answers to the above questions concerning the inevitability and uniqueness of magnetic domains are given.

Of course, the situation in which external fields are applied has great practical significance. It should be incorporated into a theoretical framework in order to cover the development of the **M** distribution as a function of the external field. For this purpose, a less ambiguous local approach is adopted in which the relationship between the mutual domain-wall positions that have one region in common—the cluster knot—and the **M** distribution outside the wall regions in the immediate vicinity of the cluster knot is determined. The collection of all domain walls that have one specific cluster knot in common is referred to as a domain-wall cluster. With the cluster concept, a better interpretation of the domain-structure observations by means of the Bitter, SEM, and Kerr techniques is possible. It also improves the understanding of Lorentz images in the ripple-free films, where no direct information is gained about the **M** distribution within the domains. In terms of the domain-wall clusters, each domain structure can be considered as a concatenation of interconnected wall clusters, in which each cluster provides local information about the **M** distribution that can be mutually correlated in order to reconstruct the **M** distribution in the entire object. When an external field induces changes in the **M** distribution, wall clusters are added to the already existing domain structure in some phases of the domain-structure progression, while they disappear during other periods. How these alterations in the number of wall clusters can take place in a reversible fashion is briefly reviewed.

As emphasized previously, the multitudinous domain structures are often reflected at the macroscopic level as hysteresis. Which of the possible domain structures develops itself depends on the prehistory in the magnetic sense. Employing the above principle, general characteristics in the domain-structure development are indicated, and the implications of these characteristics for the irreversible part of the transformations are discussed. These principles are elucidated by considering, in detail, the domain conversions in rectangular thin-film specimens.

## 2. Divergence-free two-dimensional domain structures in plane-parallel thin-film objects

In this section, the two-dimensional domain structures in ideally soft-magnetic plane-parallel thin-film objects with cylindrical edges perpendicular to the film plane are the subject of study. Here we consider only magnetization configurations which are not exposed to an externally applied magnetic field. As will be seen, two-dimensional **M** distributions in which **M** does not change in the direction perpendicular to the film plane ($z$-axis) are only possible when the external field is zero and when the object does not carry conduction currents. Moreover, it is assumed that the object's dimensions are large in comparison with the object's single magnetic domain dimensions. Under these circumstances, the author reconsidered the micromagnetic equilibrium equations and stability conditions for the class of ideally soft-ferromagnetic specimens. In this kind of medium the intrinsic anisotropy is set at zero, because the magnetic energy density $\mu_0 M_s^2$ is much larger than its anisotropic counterpart. In the domains, the spatial variation term in the exchange-energy density can be safely neglected. Hubert [21, 22] and LaBonte [23] demonstrated that this exchange term constitutes a second-order effect even in the domain-wall regions of soft-magnetic media. Therefore, in first-order approximation, both coupled partial differential equations defining the equilibria reduce [24] to

$$\mathbf{H} = C(x, y, z)\mathbf{M}, \tag{1a}$$

$$\mathbf{M} \cdot \mathbf{M} = M_s^2, \tag{1b}$$

while their stability is guaranteed when

$$C(x, y, z) \geq 0; \tag{1c}$$

**H** is the total Maxwell field and **M** and $M_s$ are the magnetization vector and its magnitude, respectively. As emphasized above, we shall confine ourselves to the situations where both the external field and the conduction currents in the object are zero. In the same order of approximation as (1), the total energy $G$ is given ([25], p. 154) by

$$G = -\frac{1}{2}\mu_0 \int \mathbf{H}_d \cdot \mathbf{M}\, dV = \frac{1}{2}\mu_0 \int_{\text{all space}} \mathbf{H}_d \cdot \mathbf{H}_d\, dV,$$

where the integration is over all space, and which is minimal when the demagnetizing field $\mathbf{H}_d$ is zero, so that

$$\nabla \cdot \mathbf{M} = \frac{\partial M_x}{\partial x} + \frac{\partial M_y}{\partial x} = 0 \tag{2a}$$

within the object volume $V$, and

$$\mathbf{M} \cdot \mathbf{n} = 0 \tag{2b}$$

on $S$; $V$ defines the space occupied by the object, and $S$ and **n** respectively denote its bounding surface and the outwardly pointing unit vector normal to $S$. $M_x$ and $M_y$ are the lateral **M** components with respect to a Cartesian coordinate system. Relations (1) and (2) are the key equations of the present theory.

• *Ambiguities in M*

Since we confine ourselves to the two-dimensional **M** distributions in which **M** is constrained to lie in the film plane, we need only consider the projection of **M** onto the $x$–$y$ plane. One of the dependent variables in (2a) can be removed by virtue of constraint (1b), substituting

$$M_x = \mathbf{M}_s \cos\phi \tag{3a}$$

and

$$M_y = \mathbf{M}_s \sin\phi, \tag{3b}$$

where $\phi$ is the angle of the magnetization direction with respect to the positive $x$-axis in the $x$–$y$ plane. Then Equation (2a) transforms into

$$-\frac{\partial\phi}{\partial x}\sin\phi + \frac{\partial\phi}{\partial y}\cos\phi = 0, \tag{3c}$$

which can also be written as

$$-p\sin\phi + q\cos\phi = 0, \tag{3d}$$

being a quasilinear first-order partial differential equation of the general form

$$G(x, y, \phi, p, q) = 0. \tag{3e}$$

The so-called characteristics of Equation (3d) are defined by the following set of ordinary differential equations (see [26], pp. 61–66):

$$\frac{dx}{dt} = \frac{\partial G}{\partial p} = -\sin\phi, \tag{4a}$$

$$\frac{dy}{dt} = \frac{\partial G}{\partial q} = \cos\phi, \tag{4b}$$

$$\frac{d\phi}{dt} = p\frac{\partial G}{\partial p} + \frac{\partial G}{\partial q} = 0, \tag{4c}$$

$$\frac{dp}{dt} = -\frac{\partial G}{\partial x} - p\frac{\partial G}{\partial \phi} = p^2\cos\phi + pq\sin\phi, \tag{4d}$$

$$\frac{dq}{dt} = -\frac{\partial G}{\partial y} - q\frac{\partial G}{\partial \phi} = pq\cos\phi + q^2\sin\phi, \tag{4e}$$

where $t$ is a position parameter along the characteristics. Equations (4a)–(4e) define a family of curves in the $(x, y, p, q, t)$ space which are given by the intersection of the following set of hypersurfaces (see [26], pp. 10–15):

$$u_1 = x\cos\phi + y\sin\phi = C_1, \tag{5a}$$

$$u_2 = \phi = C_2, \tag{5b}$$

$$u_3 = \frac{p}{q} = C_3, \tag{5c}$$

$$u_4 = t\sin\phi + x = C_4, \tag{5d}$$

$$u_5 = y - x + \frac{p+q}{p^2+q^2} = C_5. \tag{5e}$$

Equations (5a) and (5b) show that each characteristic base curve, being the projection of the characteristic onto the $(x$–$y)$ plane, is a straight line with the magnetization perpendicular to it. The boundary condition, given by (2b), prescribes an alignment of the dipoles parallel to the edge to prevent surface charge from occurring. Hence, the characteristic base curves are straight lines perpendicular to the edge. The latter can be made plausible in the following way. The characteristic base curves are the lines in the $x$–$y$ plane along which a given **M** direction at point $P$ governs **M** on its surrounding $\Delta S$.

Let $\phi(x', y')$ define a stable differentiable **M** distribution on $\Delta S$, and let the $y'$ axis of the coordinate system with origin at $P$ be parallel to **M** at this point. Let $\Delta\phi(x', y')$ be a differentiable perturbation of $\phi$ satisfying $\Delta\phi(0, 0) = 0$. The magnetic charge density $\rho$ caused by this perturbation follows from the left member of Equation (3c) by replacing $\phi$ with $\phi + \Delta\phi$. The charge density at $P$ is given by

$$\rho = \left[\left(\frac{\partial\phi}{\partial x'} + \frac{\partial\Delta\phi}{\partial x'}\right)\sin\phi - \left(\frac{\partial\phi}{\partial y'} + \frac{\partial\Delta\phi}{\partial x'}\right)\cos\phi\right]M_s = \frac{\partial\Delta\phi}{\partial x'}.$$

This shows that the variation of **M** only in the direction normal to **M** is effective in inducing charge, charge that tends to recover the original stable situation. This direction is in compliance with the normal orientation of **M** with respect to the base curve; however, it does not prove the straightness of the latter curve.

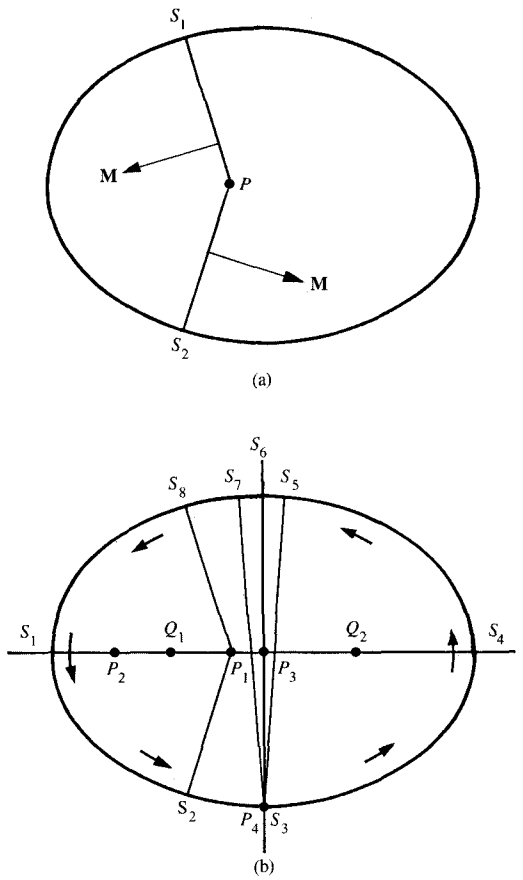


**Figure 1**

(a) The intersection $P$ of two base curves through the edge points $S_1$ and $S_2$. (b) All characteristic base curves that intersect at $P_1$ to $P_4$ in an ellipse. The initiating edge points are $S_1$ to $S_8$.

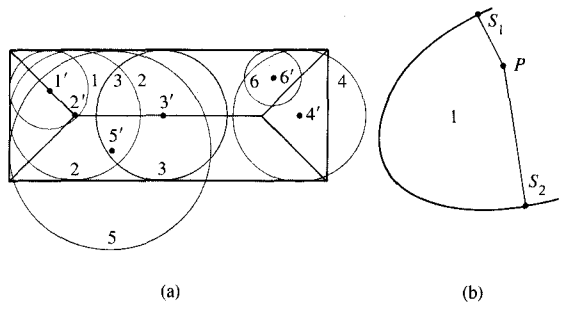


**Figure 2**

(a) Interpretation of the basic structure in terms of the locus of center of circles. (b) The position of domain-wall point $P$ with respect to the edge points $S_1$ and $S_2$.

**Figure 1(a)** shows two base curves corresponding to two edge points $S_1$ and $S_2$ that intersect in the point $P$ within the object. **M** is perpendicular to these curves, so it is obvious that the edge segments at $S_1$ and $S_2$ prescribe two incompatible **M** directions at $P$. Let us examine more closely the consequences of this straightness and of the orientation of **M**. The boundary condition $\mathbf{M} \cdot \mathbf{n} = 0$ shows that the base curves are straight lines perpendicular to the edge. In **Figure 1(b)** a number of these base curves corresponding to the edge points with parametric position coordinates $S_1$ to $S_8$ are depicted in an elliptical object. Observe that the base curves through $S_2$ and $S_8$ intersect at $P_1$ and prescribe two different directions of **M** at the same point. It is shown elsewhere [27] that similar conflicting requirements arise in the whole ellipse, where a maximum of four intersecting base curves at one point can be found in some regions. Thus, we are faced with an ambiguity in **M**, which is a result of the incompatibility of the continuous **M** distributions that are imposed by and extend themselves from the various edge segments. This nonphysical multiplicity in **M** can be dealt with only by allowing discontinuities in **M** along lines [27, 28], i.e., by allowing domain walls such that the **M** distributions imposed by the various edge segments can be separated and matched. The simplest domain structures—the so-called basic structures—that can accomplish this task are treated in the next section.

• *The basic domain structures*

As stated previously, domain walls appear in the two-dimensional images as curves across which **M** and the attendant base curves perform a discontinuous jump in their direction. To preserve the solenoidality of **M**, the component of **M** normal to the wall surface has to be continuous across this surface; i.e., the bisector relation applies ([25], Ch. 5). As a result, the tangent to the domain wall at any point $P$ not at the extremity of the wall is parallel to the bisector of the base-curve segments with extremities at $P$ and the edge points at which they originate.

The domain-wall pattern and the dipole distribution of the basic structure in objects with an arbitrary lateral shape can be rigorously derived by using differential geometry [28]. Here we confine ourselves to stating without proof the ultimate conclusion and to discussing this result. It was proved [28] that the domain walls of a basic structure constitute the locus of all the centers of circles that, first, touch the object edge at at least two points and that, second, are completely situated within the object.

We illustrate this law with the well-known Landau–Lifshitz structure in a rectangular platelet [see **Figure 2(a)**]. The circles marked 1, 2, and 3 touch at minimally two points at the edge and lie completely within the

platelet, so that their centers, 1′, 2′, and 3′, respectively, are located at the domain walls. Note that circle 2 is touching the edge at three points, implying that its center 2′ coincides with a free domain-wall cluster knot (see [23], Ch. 4). Circle 6 is also completely situated within the platelet; however, it touches the edge at one point only, so that its center 6′ does not belong to the locus.

Opposite to this, circles 4 and 5 are touching at sufficient edge points; however, they are lying only partly within the object, so that centers 4′ and 5′ are not at domain walls. Having thus elucidated the law, let us turn our attention to an attempt to comprehend certain of its aspects. **Figure 2(b)** shows point $P$ at a domain wall, together with both base lines that interconnect $P$ with the edge points $S_1$ and $S_2$. We apply the Gaussian law to Part 1 of the object, which is bounded by the edge and base lines $PS_1$ and $PS_2$. Bear in mind that **M** is parallel to the bounding surface of the object, so that

$$\int\int\int_{\text{Part 1}} \nabla \cdot \mathbf{M}\, dv = 0,$$

and therefore,

$$\int\int_{PS_1} \mathbf{M} \cdot \mathbf{n}\, dS + \int\int_{PS_2} \mathbf{M} \cdot \mathbf{n}\, dS = 0.$$

From this it follows that $PS_1$ and $PS_2$ are of equal length, because the objects are plane parallel and thus have a constant thickness, and because **M** is normal to the characteristic base curves. The circle with radius $PS_1$ and center $P$ touches the edge at $S_1$ and $S_2$ because the tangents to the edge at $S_1$ and $S_2$ are perpendicular to $PS_1$ and $PS_2$, respectively. Note that this does not imply that the circle is completely situated within the object.

Let us focus on a second consequence of the law and take a look at the extremities of the domain walls. **Figure 3(a)** shows one single domain wall along the symmetry axis of an ellipse which clearly constitutes the basic structure of Figure 1(b). The edge points $S_1$ and $S_4$ of Figure 1(b), which correspond via the base curves to the wall extremities $Q_1$ and $Q_2$, demarcate two edge segments, imposing two (in principle) incompatible **M** distributions, which are matched at the domain wall. Obviously, the wall at $Q_1$ separates the base curves corresponding to the edge points at infinitesimal distances from $S_1$ and on both sides of $S_1$. The base curves mentioned above intersect at $Q_1$, so that $Q_1$ is the center of curvature of the edge at $S_1$. It can easily be understood that the radii of curvature are locally minimal at $S_1$ and $S_4$. In general [28], each extremity of a domain wall in a basic structure that does not coincide with extremities of other walls is located at the center of the radius of curvature of a convex edge segment with a locally minimal radius. In the case of edges with vertices,

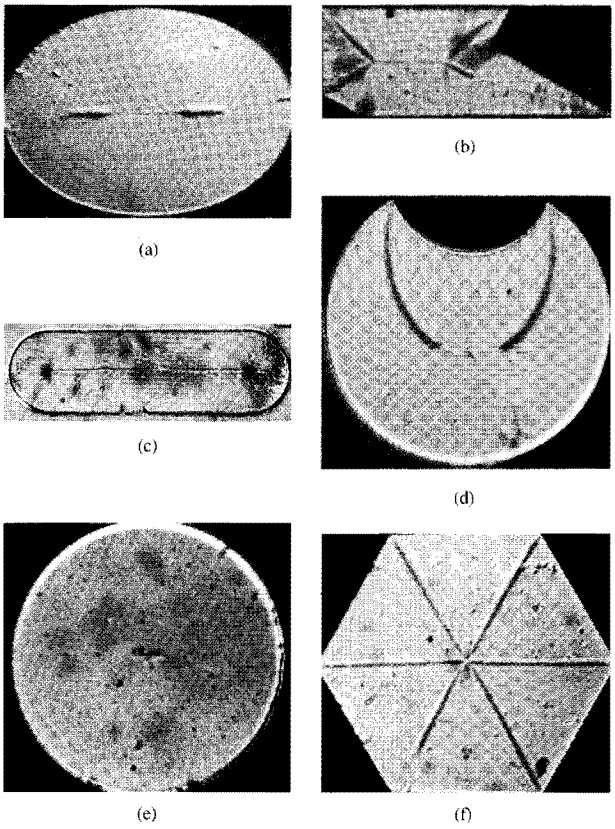


**Figure 3**

Ferrofluid patterns of basic structures in Permalloy thin-film elements with various lateral shapes. Dimensions of the specimens, 50 to 100 $\mu$m; thickness, 2500 Å.

as in the rectangular platelet, these centers of curvature coincide with the vertices. The requirement of convexity to the edge segment follows from the fact that the base curves of concave edge segments have no points of intersection in the region adjacent to this segment where **M** is governed by this segment. An example is provided by **Figure 3(b)**, where no domain wall adjacent to the sole concave vertex betrays itself, while, opposite to this, each convex vertex has its wall. **Figure 3(c)** shows the positions of the wall extremities in the case of two convex edge segments.

The degenerated domain structure in the circular object of **Figure 3(d)** deserves special attention. In this case, the family of circles mentioned above reduces to one single circle, namely the circular contour of the object, so that the wall configuration simplifies to one single point in the object center. One single domain wall matches the **M** distributions imposed by both circular segments in **Figure 3(e)**. It has been proved elsewhere [29] that this wall possesses an elliptical shape. Finally,

(a)

(b)

**Figure 4**

Kerr observations of basic domain structures in rectangular Permalloy thin-film specimens. Dimensions: (a) 20 × 50 $\mu$m, (b) 50 × 50 $\mu$m; thickness of both specimens $\simeq$ 350 Å. (Courtesy of B. Argyle and coworkers, IBM T. J. Watson Research Center, Yorktown Heights, NY.)

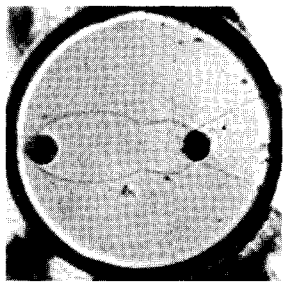

(a)

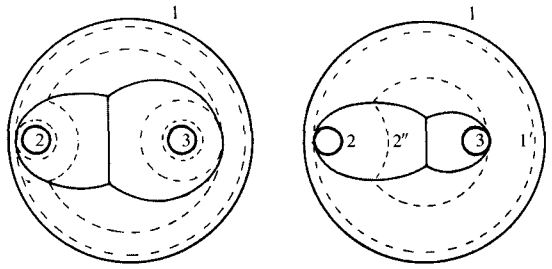


**Figure 5**

(a) A multiply connected Permalloy specimen with an outer diameter of 50 $\mu$m and film thickness of 2500 Å. (b) The corresponding basic configuration. (c) Construction of the actual domain structure with shorter wall length.

the symmetrical configuration in a regular hexagon is shown in **Figure 3(f)**. **Figures 4(a)** and **4(b)** show the basic structures in rectangular Permalloy samples, as observed by Argyle and coworkers by means of their Lamon–Kerr system, in which the **M** distributions within the domains can also be discerned. The agreement with the predicted **M** distributions is completely satisfactory. Additional examples of basic structures can be found in [30–34].

Until now, only simply connected objects have been discussed. **Figure 5(a)** provides an example of a simple domain structure in a multiply connected object (an object with one or more holes) which is not a basic structure. The corresponding basic structure is shown in **Figure 5(b)**. Note that it is characterized by a greater wall length in comparison with Figure 5(a), and that the actual **M** distribution exhibits a smaller energy, and, in good approximation, is also solenoidal (divergence-free). The observed structure is an example of the so-called composite structures coming up for discussion in the next sections. How this minimal wall-length configuration can be systematically constructed is described in [28] [see also **Figure 5(c)**]. A more dramatic reduction in the wall length in comparison to the basic structure is observed in the ring-shaped object of **Figure 6**. The inner edge of this object runs perpendicular to the characteristics stretching out from the outermost edge, so that no conflicting dipole distributions are imposed by the inner and outer edges. Moreover, note that the characteristic base curves intersect in the center of the ring, where no magnetic material is present. Therefore, the origin of the conflicting requirements to **M**, by which the domain walls become inevitable, is removed. This ring constitutes an important case, for it is a preeminent example of the so-called parallel regions discussed in the next section.

• *The composite domain structures*

In the foregoing sections, we have been faced with the inevitability of domain walls as a consequence of the nonlinearity of Equation (3) due to the constraint $\mathbf{M} \cdot \mathbf{M} = M_s^2$. In this section, this nonlinearity also emerges as the origin of multiplicity in the domain structure. To demonstrate this nonuniqueness, we decompose the area of the object by defining auxiliary

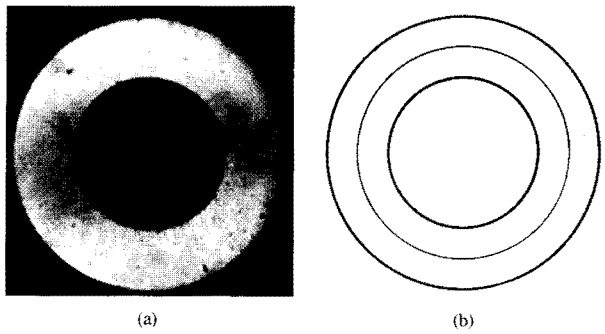

(a) (b)

**Figure 6**

(a) Ring without domain structure. (b) Basic structure in a Permalloy ring with an outer diameter of 50 $\mu$m and film thickness of 2500 Å.

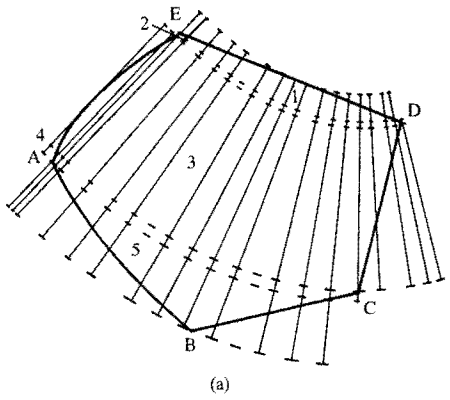


(a)

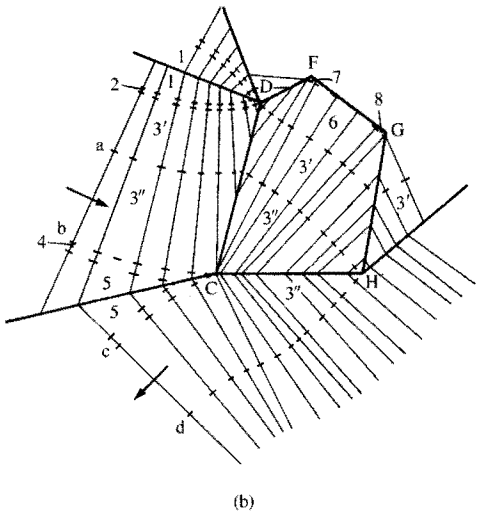


(b)

**Figure 7**

(a) Decomposition of domain ABCDE into regions bounded by the parallels through the cluster knots A, C, D, and E. (b) Further decomposition of region 3 by cluster knot H.

edges into a number of disjunct subregions whose union completely covers the object. In each subregion, we define a solenoidal **M** distribution with **M** parallel to the boundaries of the subregion. Of course, these solenoidal distributions do not mutually interfere via magnetic fields, so that such a decomposition is always allowed, and the aggregation of the subdomain structures is a feasible configuration in the object. In order to cover all domain structures possible, we shall again examine the general characteristics of the **M** distributions in the domains.

We elaborate a general procedure in the following subsection by which a unique decomposition of the object into disjunct subregions that completely cover the specimen is accomplished. This decomposition into subregions is completely defined by the **M** distribution. A procedure is subsequently outlined from which all feasible subregions can be derived that cover any arbitrary thin-film object, and that defines domain structures satisfying our requirement of solenoidality.

*Decomposition into subregions*

In **Figure 7(a)**, we have depicted domain ABCDE, which exhibits no interior domain-wall configuration, so that the characteristic base lines (denoted by the thin lines) defining **M** in this domain have no points of intersection here. Moreover, we have plotted all orthogonal trajectories (the dashed curves) of this family of base lines that pass through the cluster knots A, B, C, D, and E (see Section 1 for the definition of a cluster knot) and all trajectories that touch at domain walls. Note that these trajectories coincide with field lines of the **M** vector field and are parallels in the geodesic sense, and that the decomposition of the domain area is uniquely defined. Each pair of adjacent parallels bounds a region, a so-called parallel superregion, with a specific width, which is the geodesic distance between the parallels measured along the base curves.

Let us trace the production of the parallel superregion 3 across wall CD. It was emphasized previously that the bisector relation applies to the **M** jump across the wall, so that the base curves of domain ABCDE intersecting wall CD transpose uniquely into base curves in domain CDFGH. The parallels bounding region 3 are produced in domain CDFGH without changing the width of region 3 [see **Figure 7(b)**]. Note that region 3 contains cluster knot H, where the flux of this region bifurcates. Therefore, 3 is further decomposed into 3′ and 3″. This

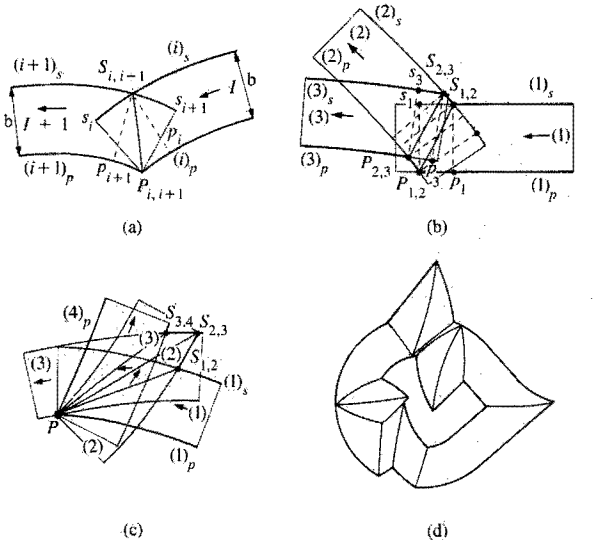


**Figure 8**

(a) Separating domain wall between two adjacent segments $(i)$ and $(i + 1)$. (b) The coupling of three successive segments. (c) The coupling of four parallel segments whose points of intersection at the $p$-edges coincide. (d) A complete parallel subregion and its domain walls.

decomposition also extends itself into the original domain ABCDE, so that the widths of the subregions 3′ and 3″ are preserved through all domains, provided no further bifurcation at cluster knots or at domain walls in other domains takes place. When 3′ contains a cluster knot in some domain, a further decomposition is carried out. In this way, a unique decomposition into subregions bounded by parallels can be specified for any solenoidal two-dimensional **M** distribution. (Situations not covered above are treated elsewhere [35].)

Let us examine more closely one such subregion, e.g., 3″ in **Figure 7(b)**. Assume that this region is not further subdivided by a cluster knot; if this is not the case, we consider region 3‴ that satisfies this condition. In Figure 7(b), we consider the segment abcd of 3″. At the characteristic through a and b, **M** is assumed as indicated by the arrow, so that **M** at line cd can only have the marked direction normal to cd. Evidently, line cd cannot coincide with the object edge, so there must exist another segment cdef of 3″ that meets segment abcd at line cd. Thus, line cd is replaced by ef. However, the same argument for the extension of abcd applies also to abef. Therefore, an impeding expansion of the number of segments of 3″, and, along with this, an unbridled growth of the 3″ area, can only be warded off by allowing line gh to coincide with ab.

In other words, 3″ and thus all subregions are bounded by two (or in special cases by one) closed curves, which are orthogonal trajectories of the characteristic base lines. In principle, the **M** distribution in these multiply connected regions bounded by two of these curves—the so-called parallel (sub)region—is not yet known, while the simply connected ones bounded only by one closed curve contain the well-known basic structures. Hence we are able to construct all solenoidal **M** distributions possible when a general procedure for the derivation of the parallel regions and their **M** distributions is at our disposal. This is the main theme of the following section.

*Parallel subregions*

As discussed, a parallel subregion is a multiply connected ringlike area bounded at both sides by parallels, which are orthogonal trajectories of the base curves. A specific width can be attributed to each parallel subregion. We compose each parallel subregion by combining basic units—the so-called parallel segments—where the width of the parallel segments is equal to the width of the parallel subregion under consideration. The magnetization in a parallel subregion has a specific rotation sense, and the segments of the subregion are consecutively numbered in compliance with this sense. How the adjacent segments in such a ring are linked and what restrictions apply are outlined only roughly here; for further details the reader is referred to [35]. We now define a parallel segment.

A parallel segment is a region with a continuous **M** distribution that is enclosed by two parallels of a family of straight characteristic base lines and two of these base curves at both ends [see **Figure 8(a)**]. The parallels of segment $(i)$ are denoted by $(i)_s$ or $(i)_p$ depending on whether they are on the right-hand or left-hand side, respectively, of the arrow indicating the circulation sense. Clearly, both corresponding edges of two successive segments have to intersect; however, they may also touch each other pairwise. In the latter case, the base curve that passes through both points of contact of both corresponding edges constitutes the intermediate boundary between the effective parts of segments $(i)$ and $(i + 1)$. Note that the union of these parts is again a parallel segment, so that the definition in this case $(i + 1)$ does not make much sense. Figure 8(a) presents the opposite situation with two points of intersection $S_{i,i+1}$ and $P_{i,i+1}$. Here, the **M** distributions of segments $(i)$ and $(i + 1)$ are matched by the domain wall running between $S_{i,i+1}$ and $P_{i,i+1}$. It is shown elsewhere [35] that this wall is the locus of centers of circles that touch both at segment $S_{i,i+1}S_i$ and at $S_{i,i+1}S_{i+1}$ or, alternatively, that touch both at segment $P_{i,i+1}P_{i+1}$ and at $P_{i,i+1}P_i$. Herein,

each pair of points ($S_{i,i+1}$ and $S_i$), ($S_{i,i+1}$ and $S_{i+1}$), ($P_{i,i+1}$ and $P_i$) and ($P_{i,i+1}$ and $P_{i+1}$) is located on the same characteristic base line.

Consider the three successive segments (1), (2), and (3) [see **Figure 8(b)**]. Of course, we can express the separating wall between each pair of adjacent segments in terms of a locus of centers of circles. However, both domain walls are not mutually independent. They should arise in the right sequence and should not have points of intersection. This requirement is satisfied when the points of intersection of the corresponding edges have the correct sequence, and, in addition, when the edge segment $S_{2,3}S_3$ does not intersect its pendant $S_{1,2}S_1$. The necessity of the latter requirement is proved in Appendix A; however, that such a relationship exists can be intuitively seen by bearing in mind the following. The edge segments $S_{2,3}S_3$ and $S_{1,2}S_1$ together with edge $(2)_s$ determine the course of the walls between parallel segments (3) and (2) and of the one between segments (2) and (1), respectively. Of course, for reasons of symmetry, a similar restriction applies to edges $(1)_p$ and $(3)_p$.

The region of segment (2) between the above walls is denoted as $\pi_2$. The chain of segments in the parallel subregion can be extended at will on the condition that $\pi_1 \cap \pi_2 \cap \cdots \cap \pi_n = 0$, where $n$ is the total number of segments of the subregion.

We examine briefly one important particular situation. Observe that three walls meet at cluster knot C in Figure 7(b). Thus, three segments of region 3″ have one point in common at the segment edges at this vertex of 3″. Such a configuration can be considered as a degeneration of the situation of Figure 8(b), when $P_{2,3}$ and $P_{1,2}$ coincide in the limit. Note that $P_{2,3}$ and $P_{1,2}$ still arise in just the correct order. Of course, the restrictions to the shapes of the segment edges, as discussed above, apply again. In general, we are not restricted to a number of three parallel segments with one common edge point. **Figure 8(c)** shows a combination of four segments. However, it can be shown by the cluster relations [35] (see also the subsection on corner clusters) that this number of segments must be even when the vertex angle inside the parallel subregion is smaller than $\pi$.

A degeneration of the above situation presents itself when we take the vertex angle equal to $\pi$; i.e., the vertex is replaced by a continuous edge. From the edge-cluster relations [35] (see also the subsection on edge clusters), it can be seen that the number of parallel segments is even and larger than two. An example of a complete parallel subregion in which these types of segment combinations can be observed is given in **Figure 8(d)**.

*Construction of the composite structures*

We now recapitulate the principal findings of the previous sections. The decomposition of the area of the object into a number of disjunct subregions that completely cover the object has been introduced. Two different kinds of subregions have been distinguished: first, simply connected subregions in which the basic domain structures are present, and second, multiply connected parallel regions with their associated dipole distributions. It has been shown that any solenoidal two-dimensional **M** distribution possible in thin-film objects can be described in terms of united subregions with either basic or parallel configurations. Therefore, a general procedure by which any parallel subregions can be constructed suffices to cover all possible dipole configurations.

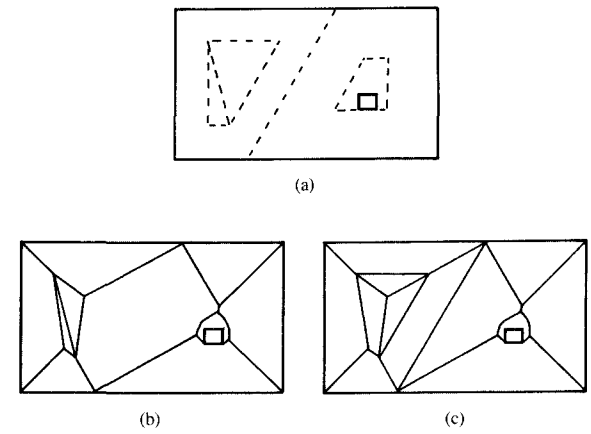


**Figure 9**

(a) Decomposition of the object into subregions. Auxiliary edges are indicated by the dashed lines. (b, c) Two of the domain structures corresponding to decomposition (a).

The starting point in this construction is the parallel segment. A parallel segment is bounded by two field lines of the **M** vector field, the parallels, and, at each end, by one characteristic base line. The parallels have continuous directional derivatives, and, measured along the characteristic base curves, the edges have constant distance, namely the segment width. A parallel subregion is a combination of overlapping parallel segments with equal width that constitute a ring-shaped closed configuration. Either two adjacent segments are coupled by one domain wall that interconnects the points of intersection of corresponding parallels, or a continuous transition exists in the case where the parallels of both segments touch pairwise. The various segments separating domain walls cannot intersect each other and

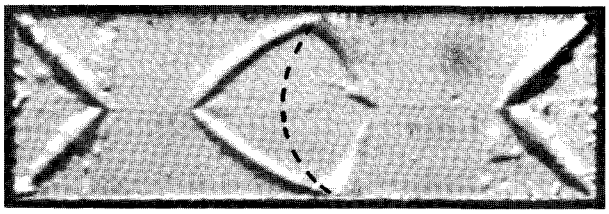

(a)

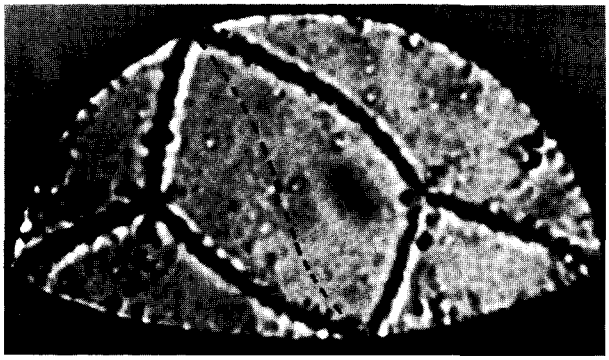

(b)

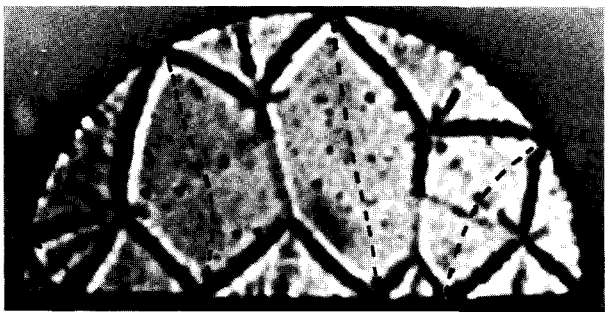

(c)

**Figure 10**

A number of composite structures in which the object decomposes into a number of simply connected subregions. The dashed lines indicate the auxiliary boundaries of the subregions: (a) Permalloy ($60 \times 20$ $\mu$m, thickness 2500 Å); (b, c) Permalloy (60 $\mu$m, thickness 2500 Å).

can only have their extremities in common. In the latter case, regions arise that, at first glance, can hardly be recognized as parallel regions [see Figure 8(d)].

During the construction of the parallel configurations, we have assumed a specific circulation sense of **M**. It is obvious that the ultimate shape of the parallel subregion and its domain-wall configuration are equally valid when the circulation sense is the opposite. Similarly, the basic wall configuration in simply connected subregions does not depend on the circulation sense. On the other hand, a 180° wall must arise at the intermediate boundary between adjacent subregions with opposite **M** on both sides of the intermediate boundary, so that the domain-wall configuration is positively affected by the circulation senses in the various subregions. Given only the shapes of the $n$ subregions in which the object is decomposed, $2^{n-1}$ different wall configurations are possible. A few examples are provided by **Figures 9(a)–9(c)**, where two of the sixteen possible configurations are shown. In this, the auxiliary edges are indicated by dashed lines. In **Figure 10**, three examples of Bitter patterns are given in which the composite structures are simply the composite of a number of basic structures in a simply connected subregion whose auxiliary boundaries are, again, indicated by the dashed lines. Of course, each of these basic structures is again the locus of centers of circles that touch minimally at two points of the corresponding subregion's boundaries and are completely situated within that particular subregion. A Kerr image of the same type of composite structure is provided in **Figure 11(a)**, while **Figure 11(b)** shows a composite structure in the P1 layer of a thin-film head as observed by A. Hubert and coworkers (Siemens A. G., Erlangen, FRG, private communication).

Composite structures with greater complexity in which parallel subregions also show up are presented in **Figure 12**. The domain structure of Figure 12(a) in a thin Permalloy layer exhibits two cross-tie types of substructures. The area of the object is decomposed into three simply connected subregions along the sample's central axis and two parallel subregions. In particular, the outermost parallel subregion is composed of a large number of parallel segments, which are coupled in a rather complex fashion. Figure 12(b) shows an interpretation of DeBlois's observation of a composite structure (see Figure 11 of [36]). This structure catches the eye because two "floating" domain walls are present with unconnected extremities in the middle of the specimen. The fundamental possibility of such situations is elucidated by the simply connected subregion of the dumbbell type, which contains two concave segments. Figure 12(c) shows another example of a complex composite structure borrowed from DeBlois (see Figure 32 of [37]), which demonstrates the validity of the procedure presented above for specimens in which the impact of the anisotropy is distinctly visible. References [2, 33, 36–42] represent an arbitrary selection from the literature with photographs of composite structures in thin-film elements, and [43–48] of this kind of domain configurations in soft-magnetic whiskers.

• *Discussion of the solenoidal domain structures*

From the above examples, it can be concluded that we are faced with an overwhelming variety in structures and also in actual objects. All of these structures in a specific object have the same energy when the anisotropy and wall energy are neglected. Transformations between these

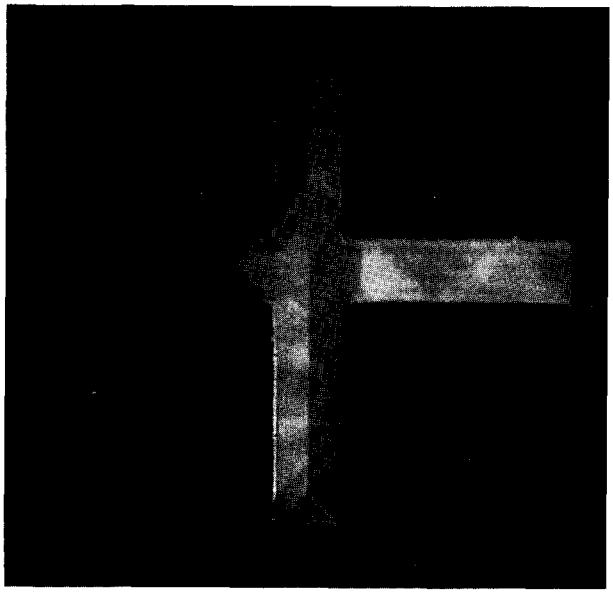

(a)

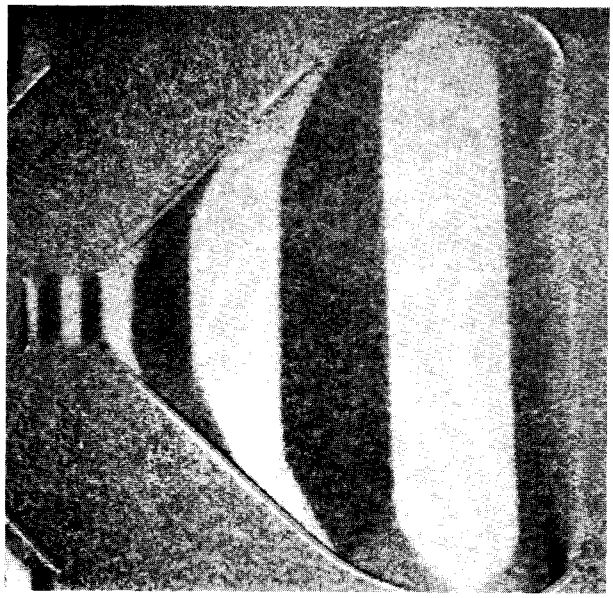

(b)

**Figure 11**

Kerr image of composite structures: (a) An array composed of basic substructures (courtesy of B. Argyle and coworkers, IBM T. J. Watson Research Center, Yorktown Heights, NY). (b) The P1 layer of a thin-film head, length 100 $\mu$m, thickness 5000 Å (courtesy of A. Hubert and coworkers, Siemens A.G., Erlangen, FRG).

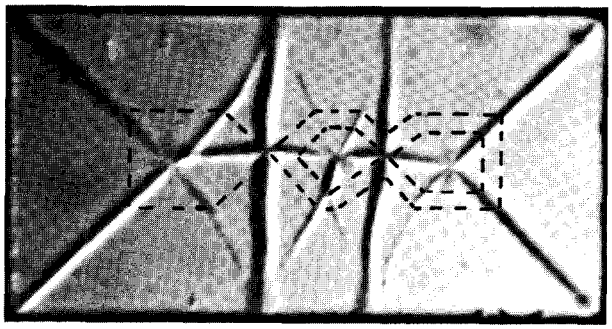

(a)

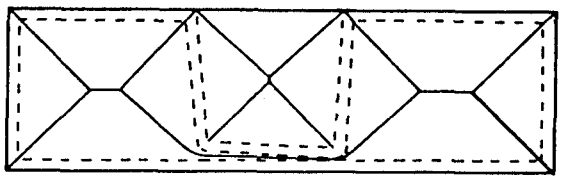

(b)

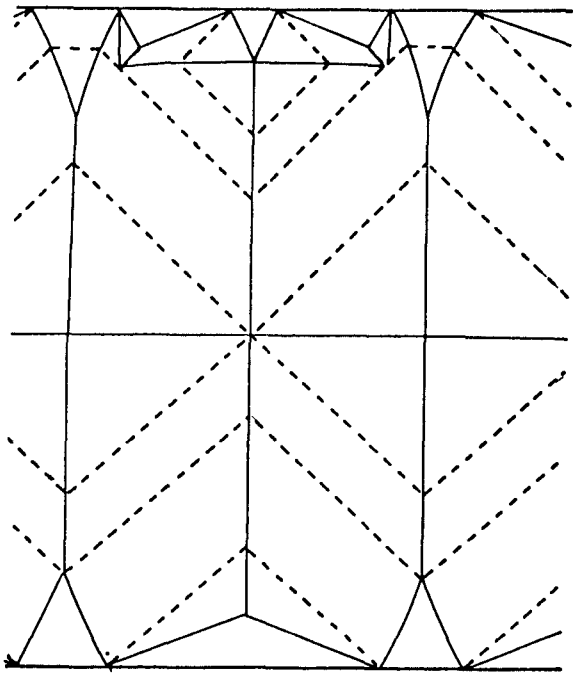

(c)

**Figure 12**

Composite domain structures with parallel subregions: (a) Permalloy specimen (60 × 30 $\mu$m, thickness 2500 Å). (b) Interpretation of domain structure of Figure 11 from [36]. (c) Interpretation of domain structure of Figure 32 from [37].

solenoidal configurations can be realized by gradually varying the shapes and distribution of the subregions, on the condition that the geometrical rules for the parallel regions remain obeyed. No energy barricade is erected against these conversions, which, therefore, are reversible.

The latter need not necessarily be true when an external field is present, because the **M** distributions are no longer solenoidal. There are strong experimental indications [49] that there exists a close correlation between the domain structure and the distribution of the Maxwell field, and that the latter penetrates the domains. As a consequence, the system's energy for a given external field will likely depend on the domain structure. A similar dependence on the domain geometry was observed in garnet layers, where it leads to topological hysteresis [50], in which, however, the domain-wall energy also plays an essential part. Even so, the wall-stray fields in soft-magnetic elements may result in a net hysteresis [51] (see also Section 4).

In the ideally soft-magnetic objects, these wall-stray fields originate in the domain-wall cores, where the torques due to the first-order variation in the exchange energy, which is not covered by constraint (1b), are counterbalanced by magnetic fields. However, there is a much more obvious reason that accounts for differences in the energy among the various domain structures.

Until now, no attention has been paid to the impact of the anisotropy energy upon domain structures. This energy will certainly be different for the various domain structures in a given sample. In elements with small lateral dimensions, there is a tendency toward domain structures with a minimal wall length, i.e., toward basic structures in simply connected objects. This can be explained as follows. Given a certain lateral shape, the wall and anisotropy energy are a linear and a quadratic function of the linear scaling factor of the lateral dimensions, respectively. Therefore, the anisotropy energy dominates in objects with large lateral dimensions and thus tends to enforce complex structures—the composite structure—in order to reduce the area of domains with an unsuitable **M** distribution. Experimental support of this statement is abundantly provided by, e.g., the previously cited works of DeBlois [36–37].

A brief discussion of DeBlois's [37] broad view of the order in the domain structure is called for. He defined topological diagrams involving a number of closed loops in the domain structure along which there is flux closure. It is self-evident that these closed loops resemble the parallel subregions. On the other hand, in general, each DeBlois loop contains a number of parallel and simply connected subregions. However, DeBlois's approach is meant as a schematic analytic tool and is not an attempt to predict the possible domain-wall configurations in his rectangular thin-film objects.

A discussion of the work of Williams [52], who confined himself to domain structures in ideally soft-ferromagnetic thin-film elements with polygonal lateral geometry, is also timely here. His domain configurations exhibit a very close resemblance to the basic domain structures presented in this paper; however, differences reveal themselves in the case of objects with concave edge segments. In the polygonal simply connected segments to which Williams confines himself, this situation presents itself as soon as vertices are present that cover an arc larger than 180° inside the specimen. In this situation, the basic structures have shorter wall lengths and thus lower wall energy and are therefore more likely. It is self-evident that, because of these deviations, the Williams structures do not fit into our unifying description of the basic structure in terms of loci of centers of circles. Moreover, the present approach not only covers a wider range of object geometries but also the large variety of the composite structures. Finally, this work offers a methodology by which all possible configurations can be generated in a systematic fashion.

Let us reconsider our solenoidal domain structures from the viewpoint of topological defects [53]. In our two-dimensional projection of **M**, the domain walls constitute one-dimensional defects, i.e., lines of discontinuity in **M**. Toulouse and Kléman [54] proved that only point defects are topologically stable in a two-dimensional vector of fixed magnitude. In their view, any basic structure in simply connected objects should always contain only one point defect, having winding number one, while more point defects may arise in composite structures. The inconsistency in the conclusions of the present and the topological approach can be explained as follows. The topological theory is based on the continuous extension of **M** into the interior of a closed curve, at which a continuous **M** is defined, while, in the present theory, we impose the extra requirement of solenoidality on **M**. This implies that the above extension of **M** is subjected to an extra requirement of the solenoidality on **M**, implying that the above extension of **M** is subjected to extra restrictions. It is still an unsolved problem whether these requirements of solenoidality also require line and surface defects to occur in the three-dimensional vector fields. In the near future, an answer to this question will likely be found by means of the three-dimensional theory presented recently [55].

## 3. Domain-wall clusters and their conversions

In Section 2, we have focused on the two-dimensional divergence-free **M** distributions in the plane-parallel thin-film objects. Unfortunately, we cannot rely, in the ideally soft-magnetic objects, on the assumption of solenoidality when an external magnetic field is applied. Up to now, no theory that provides explicit solutions for the **M** distribution has been developed. This even applies to the category of the ideally soft-magnetic media, although these are governed by the relatively simple constitutive equation (1) and the Maxwell equations for the quasi-

static case. The reason for this is the nonlinearity introduced by the constraint $\mathbf{M} \cdot \mathbf{M} = M_s^2$. We therefore return to a less ambiguous local approach.

We focus our attention at those locations where the most information can be derived from observations about the **M** distribution and where extra constraints are imposed on **M**. Domain walls are the best visible magnetic features, and as a consequence those positions where a number of these domain walls meet are preeminently suitable as the object of study. Therefore, the domain-wall cluster is defined as the collection of all domain walls that have one region—the so-called cluster knot—in common. In this paragraph, we present a number of relations that correlate the mutual domain-wall positions and the dipole distribution in the domains in the immediate vicinity of the cluster knot. The mean lateral **M** component $\langle \mathbf{M} \rangle$, averaged over the film thickness, will herewith be the central parameter. The extent of the region in the lateral direction in which sufficient correlation exists is sufficiently large in comparison to the domain-wall core widths that a two-dimensional projection of the **M** distribution on the film plane suffices. Thus, the domain walls show up as simple lines.

We do not derive the formulae used, since a derivation can be found in [25]. Instead, special attention is devoted to relatively simple clusters, which are frequently encountered in practice. In this way, we hope to emphasize the usefulness of the cluster concept as an analytic tool from which much additional information can be derived. Moreover, it reveals much about the general order in the domain-structure transformations in the soft-magnetic thin-film objects.

• *Domain-wall clusters: Static properties*

We formulate a few starting points, assuming that no singularities in the magnetic space-charge density can occur within the ideally soft-magnetic objects except for their bounding surfaces, at which surface charge can be present. This implies that no net surface charge can be present at the domain-wall surfaces; i.e., the component of **M** normal to the wall surface is continuous across this surface. This introduces a relationship between the wall surface and the **M** directions at both sides, a correlation often referred to as the bisector rule.

The validity of this assumption is carefully considered elsewhere [25]; however, its ultimate origin can easily be understood. Equation (1) prescribes that outside the wall cores, the total Maxwell field **H** should be parallel to the magnetic dipoles at both sides of the wall surface. The dipole rotation across the wall surface has a discontinuous character, at which the **M** component tangent to this surface exhibits a jump. The Maxwell field **H** is continuous in a region where the magnetic space-charge density remains finite, so **H** must be zero at the wall in these circumstances. Of course, surface charge can be assumed at the wall surface; however, such a charge pattern gives rise to a discontinuity in the field component normal to the wall surface instead of parallel to the surface. It has been shown [25] that in the presence of this surface charge, it is impossible by the addition of a continuous field to obtain a situation where the total Maxwell field is simultaneously aligned along the dipoles at both sides of the wall. Therefore, the total Maxwell field is zero at the wall, and the bisector relation applies in the present idealized situation of perfectly soft-magnetic media. Of course, differences will occur due to the finite width of the actual wall cores and due to the unavoidable residual traces of intrinsic anisotropy. A rough estimation teaches us that the impact of these perturbations is the largest for domain walls with about zero wall angle. The deviation from the bisector rule in this worst case is about a few degrees from realistic layers and media.

Above, we have discussed the impossibility of surface charge at surfaces within the object. Next, we shall pay attention to line-charge singularities, and, in particular, to those that might coincide with the cluster knot. Here, a careful analysis is omitted (see [25]); rather, a display of the essential ideas is pursued. Let us focus on the dipole distribution of **Figure 13(a)**, which shows the top view of one of the simplest dipole configurations that gives rise to a space-charge singularity. This circular **M** pattern with constant radial **M** component $\langle M_r \rangle$ produces a charge density $\rho = \langle M_r \rangle / r$ within the cylinder about the cluster knot with height $h$, equal to the film thickness. Here, $r$ is the distance with respect to the cylinder axis of $P$, the point where $\rho$ is determined. By applying the Gaussian law and the relation $\nabla \cdot \mathbf{M} = -\nabla \cdot \mathbf{H}$, it can easily be seen that a discontinuity arises in the radial component $\mathbf{H}_r$ of the field **H** when passing through the cluster knot [see the diametric points $P_1$ and $P_2$ in Figure 13(a)]. Since both points $P_1$ and $P_2$ can be chosen at a very short mutual distance, the contribution $\mathbf{H}_e$ to the Maxwell field **H** of the other field sources located outside the cylinder is in good approximation equal in $P_1$ and $P_2$. Since $\mathbf{H}_r$ is opposite to $\langle M_r \rangle$ at both $P_1$ and $P_2$, it is impossible to select $\mathbf{H}_e$ such that Equation (1) is simultaneously satisfied in both $P_1$ and $P_2$. As a result, this space-charge line singularity represents no feasible dipole constellation in ideally thin-film objects. It is shown elsewhere that the same conclusion applies to the general line singularity.

An important implication of the absence of these kinds of singularities reflects itself at the cluster knot. Actually, the above paragraph leads to the conclusion that $\langle M_r \rangle$ has to be zero; i.e., no net $\langle \mathbf{M} \rangle$ flux is allowed into the cluster knot in any sector. Let us have a look at the **M** distribution near the cluster knot 0 between the domain

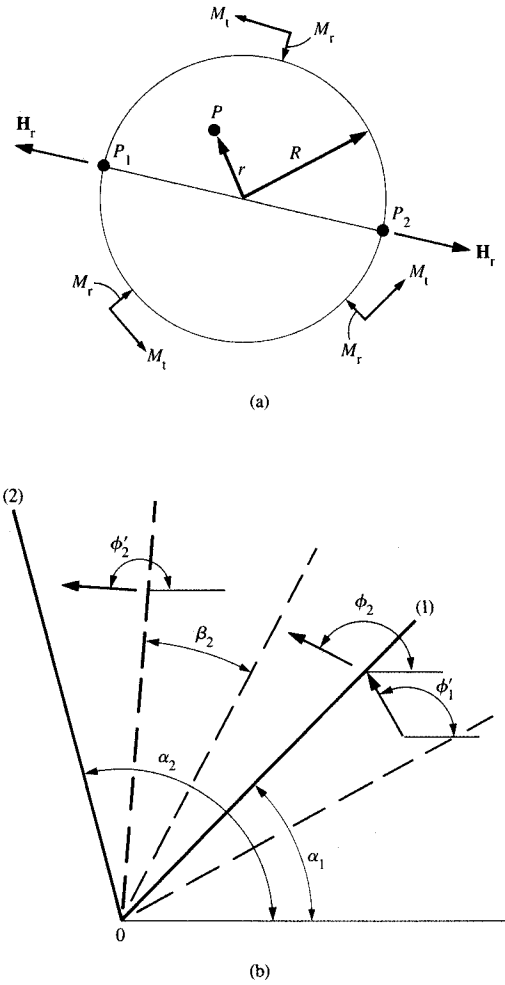


**Figure 13**

(a) A circular dipole distribution with a radial **M** component $<M_r>$ near the cluster knot. (b) The continuous magnetization modes with respect to the cluster knot 0.

walls (1) and (2) [see **Figure 13(b)**]. A jump in the **M** direction takes place at a domain wall (1). As a result, a radial **M** component is always present at both sides of this domain wall, which is ostensibly inconsistent with the above conclusion concerning $\langle M_r \rangle$. However, note that any first-order perturbation of a uniform distribution also does not focus the **M** flux in a $\rho$-divergent fashion. Therefore, two sectors—the so-called uniform sectors—extend themselves at both sides of wall (1). Each of them covers an arc $|\phi_1' - (\alpha_1 + \pi/2)|$, where $\phi_1'$ and $\alpha_1$ are respectively the $\langle \mathbf{M} \rangle$ direction at infinitesimal distance from wall (1) within the domain in question and the direction of the tangent to wall (1) at 0. Since the space-charge density is finite within such a uniform sector, the rotation of **M** across this sector declines to zero at a very short distance from cluster knot 0. Of course, a similar uniform sector bounded by wall (2) and the dashed curve at the left in Figure 13(b) is present adjacent to wall (2). Between the dashed curves, a sector—a so-called rotation segment—remains in which **M** rotates in a circular fashion about the cluster knot. Here, $\langle M_r \rangle$ reduces to zero at an infinitesimal distance from the knot (an analytic derivation is given in [25, 26]).

In conclusion, two different continuous magnetization modes have been traced for tracking the course of **M** about the cluster knot: to wit, the uniform sectors adjacent to the domain walls and the rotation segment in the middle of the domain sector between two uniform sectors, being bounded by two segment edges [the dashed curves in Figure 13(b)]. A domain that merely contains one single uniform sector with respect to a specific cluster knot 0 will be called a uniform domain of that cluster [see **Figure 14(b)**]. On the other hand, a domain that contains two uniform sectors and one intermediate rotation segment will be referred to as a rotating domain of the specific cluster [see **Figures 14(a)** and **14(c)**]. It should be noted that the sector angle $\beta$ of the rotation segment may be zero in a degenerated rotating domain [see Figure 14(a)], so that the **M** rotation across the domain sector reduces to zero near the knot; however, it is still a rotating domain, containing segment walls.

Finally, we shall put forward a classification scheme for the clusters which is based on the position of the cluster knot with respect to the object edge. This distinction is inspired by the difference in the boundary conditions that apply for clusters (see **Figure 15**) with knots located at

1. No edge—the free clusters.
2. One edge—the edge clusters.
3. Two edges—the corner clusters.

The free clusters are considered first. These are characterized by a great flexibility in the mutual domain-wall positions and in the **M** distribution that corresponds to a specific domain-wall pattern.

*The free wall clusters*

The course of the lateral $\langle \mathbf{M} \rangle$ vector through a domain near the cluster knot is determined by the mutual positions of the rotation-segment walls and the domain walls. A free cluster is a cyclical system in that the $\langle \mathbf{M} \rangle$ direction must return to the direction of departure after tracing $\langle \mathbf{M} \rangle$ at an infinitesimal circle around the knot over 360°. This constraint imposes limitations on the possible combinations of rotation segments and uniform sectors. Here, a number of these relations are merely

posed, whereas the formal proofs can be found in [25, 56, 57].

Rotation segments have been traced as one of both magnetization modes that can exist in the domains. The course of **M** through such a segment is determined on the one hand by the sector angle $\beta_i$ [see Figure 13(b)], and on the other hand by its circulation sense, which may be either clockwise or counterclockwise. It was proved that the circulation senses of the rotation segments in a specific free cluster are identical.

In the Introduction, it was emphasized that only the domain walls arise as well-delineated features in most images, whereas rotation segments are often hardly visible. This fact hampers the analysis of the free clusters. Therefore, it is interesting to know whether the uniform domains, which are lacking these rotation segments, can occur. A uniform subcluster is defined as the unbroken collection of all uniform domains in which each member has at least one domain of the collection next to it. It was proved that each uniform subcluster consists of an even number of uniform domains. Even so, a rotating subcluster has been defined as the unbroken collection of all rotating domains in which each member has at least one rotating domain of the collection next to it. Such a subcluster contains an arbitrary number of domains. Of course, the question arises whether there exist free clusters consisting merely of uniform domains—the so-called completely uniform clusters. It has been proved [25, 57] that completely uniform free clusters can exist, and that these comprise an even number of domains larger than three.

In summary, it can be concluded that three different situations can present themselves: to wit, the free cluster may be a completely uniform cluster, it may contain an equal number of uniform and rotating subclusters, or, finally, it may be a completely rotating cluster.

Across a domain wall, **M** changes jumpwise, and a specific clock-sense can be attributed to this jump, at which a specific observation direction, say from above, is presupposed [see **Figure 16(a)**]. This clock sense becomes distinctly apparent when the domain structure is visualized by Lorentz microscopy. In **Figure 16(b)**, the deflection pattern of the electron beam near both domains of Figure 16(a) is depicted. Observed from the condenser side of the microscope, the clockwise and counterclockwise domain walls appear respectively as dark and bright bands in the image. It should be emphasized that the clock sense of the walls is always discerned in the Lorentz image, while the **M** distribution in the domains is only accessible when the object exhibits ripple due to stochastic spatial variation in the physical parameters. Let us return to the clusters and have a look at Figure 14 again. Figure 14(b) shows a uniform domain, and it can be seen that the clock senses of both

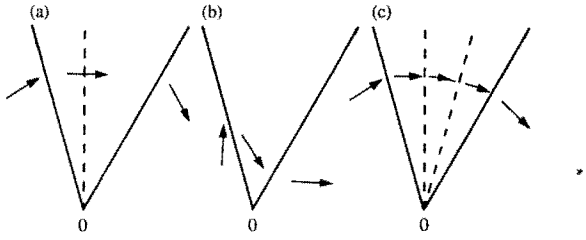


Figure 14

(a) Domain with uniform magnetization. (b) A uniform domain. (c) Determining **M** near the cluster knot of a rotating domain requires knowledge of two domain-wall and segment-wall positions.

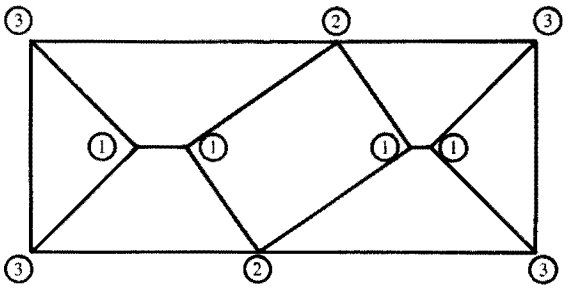


Figure 15

The classes of wall clusters: (1) Free wall clusters, (2) Edge wall clusters, (3) Corner clusters.

domain walls bounding that domain are opposite. It can be formally proved [25] that this inversion in clock sense is characteristic for uniform domains. As a consequence, a uniform (sub)cluster consists of a pattern of domain walls with alternating clockwise and counterclockwise rotation senses. In a Lorentz image, such a completely uniform cluster appears as a line pattern in which each dark line is enclosed by two bright lines, and vice versa. Returning again to Figure 14, we see that parts (a) and (c) show rotating domains in which the clock sense of both enclosing domain walls is identical. It can easily be seen that this relationship always applies for the rotating domains. Therefore, it can be concluded that each rotating (sub)cluster merely contains domain walls with one specific clock sense.

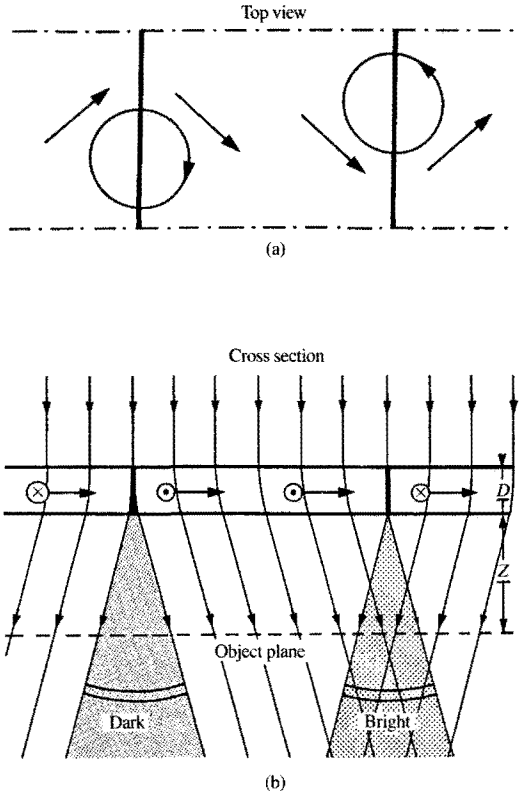


**Figure 16**

(a) The clock sense of rotation of **M** across a domain wall when viewed from the condenser lens side of the electron microscope. (b) The deflection of a parallel electron beam and the image of a domain in the object plane of the magnifying lens of the electron microscope.

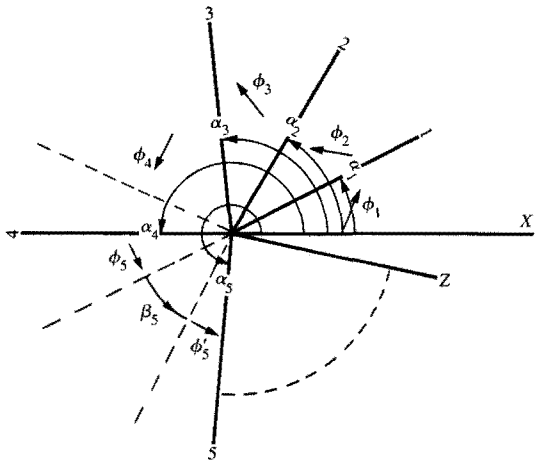


**Figure 17**

Definition of the positions of the domain walls $\alpha_j$ and the **M** directions $\phi_j$ and $\phi'_j$ in the uniform sectors of domain $(i)$.

Let us explicitly define the mutual positions of the domain and segment walls in a free cluster. The direction angles of the consecutive domain walls satisfy the inequality (see **Figure 17**):

$$0 < \alpha_1 < \alpha_2 \cdots < \alpha_{i-1} < \alpha_i < \alpha_{i+1} \cdots < \alpha_n < 2\pi. \quad (6)$$

The domain $(i)$ may contain a rotation segment, so that the directions $\phi_i$ and $\phi'_i$ of the in-plane $\langle \mathbf{M} \rangle$ components in the uniform sectors adjacent to domain walls $(i-1)$ and $(i)$, respectively, are related by

$$\phi'_i = \phi_i + \beta_i,$$

where $\beta_i$ denotes the sector angle of the rotation segment. By exploiting the bisector rule, a straightforward procedure [25] yields

$$\phi_{i+1} = \frac{\pi}{2} - (1)^i\left(\frac{\pi}{2} - \phi_1\right) + 2\gamma_1^i - \beta_1^i + 2\pi k, \quad (7a)$$

where $n \geq i \geq 0$ and $k$ is an integer. In Equation (7a),

$$\gamma_i^j = \sum_{h=i}^{j} (-1)^{(j-h)}\alpha_h \quad (7b)$$

if $j \geq i \geq 1$, for $j < i$; $\gamma_1^j = 0$,

and

$$\beta_i^j = \sum_{h=i}^{j} (-1)^{(j-h)}\beta_h \quad (7c)$$

if $j \geq i \geq 1$, but for $j < i$,

$\beta_i^j = 0$.

Note that $\phi_n = \phi_1$.

Let us apply the above rather complex formula and our previously posited general rules to the simplest possible free clusters.

The free singlet that contains one single domain wall only is the simplest cluster possible [see **Figure 18(a)**] which is always a completely rotating cluster. The rotation segment angle may vary between 360° and zero. In the latter degenerate case with $\beta_1 = 0$, the domain wall disappears, and a locally uniform **M** state is present. Two examples of these free singlets can be seen in Figure 3; in general, however, they do not tend to show up very frequently (for other examples, see [36, 37]).

The cluster next in complexity—the free doublet—contains two domain walls. It contains rotating domains only. It can be seen from Equation (7) that the rotation

segment angles $\beta_1$ and $\beta_2$ are correlated with the mutual domain-wall positions $\alpha_1$ and $\alpha_2$ by

$$\alpha_2 - \alpha_1 = \frac{(\beta_1 - \beta_2)}{2} + k\pi, \tag{8}$$

where $k$ is an integer. It follows immediately from (8) that $\beta_1 = \beta_2$ when both domain walls are in line. **Figure 18(b)** provides an example. On the other hand, both domain walls are at an angle when $\beta_1 = 0$ and $\beta_2 \neq 0$ [see **Figure 18(c)**]. **Figure 18(d)** shows the tip of a zigzag domain which frequently represents this condition [58, 59]. It is obvious that such a free doublet with one uniform domain has no reason for existence in soft magnetic media from the present point of view. When carefully observed, the image presented by Wade [60], duplicated in **Figure 19**, is presumably a more accurate representation of the tip of the zigzag wall.

Let us shift our attention to the free triplets marked by B in Figure 19. Judging from the alternation in the clock sense of the domain walls in that Lorentz image, a uniform subcluster is present in each of these clusters. Note that these uniform subclusters do indeed consist of two domains. A detailed analysis of this situation [25] indicates that such a uniform subcluster can only exist when all three domain walls are located within a sector smaller than 180°. However, it can easily be seen by comparing **Figures 18(e)** and **18(f)** that this is a necessary condition, though not a sufficient one. The triplet of **Figure 18(g)**, which is a reconstruction of the Bitter pattern of **Figure 20**, has to be the completely rotating type, judging from the arc over which the domain walls are distributed. Observe that the rotation segments betray their presence by a rippled circular distribution of ferrofluid whose centers of symmetry coincide with the cluster knot. A Lorentz photograph (**Figure 21**) provides several examples of completely free triplets, which do not satisfy the uniformity condition. In each of these clusters, the domain walls show up as a pattern of either solely dark or solely bright lines. It should be emphasized that all Lorentz observations of this kind of free triplets presented in the literature [60–64] confirm our predictions of their rotating nature. Let us determine when all domains of the triplet are uniformly magnetized. From Equation (7), it follows by putting $\phi_4 = \phi_1$ that

$$\phi_1 = \gamma_1^3 - \frac{\beta_1^3}{2} + \frac{\pi}{2} + k\pi, \tag{9}$$

which simplifies to

$$\phi_1 = \gamma_1^3 + \frac{\pi}{2} + k\pi$$

for the situation with only uniformly magnetized domains. We take $\phi_1 = 0$, so that $\gamma_1^3$ is either $\pi/2$ or $3\pi/2$. In principle, both cases are equivalent and are represented by Figure 18(e) when the only rotating domain remaining is also uniformly magnetized. Subsequently, for $\phi_1 = \pi/2$, the only situation of interest is defined by $\gamma_1^3 = \pi$ which, in principle, corresponds to the completely rotating free cluster of Figure 18(g), when all domains are uniformly magnetized.

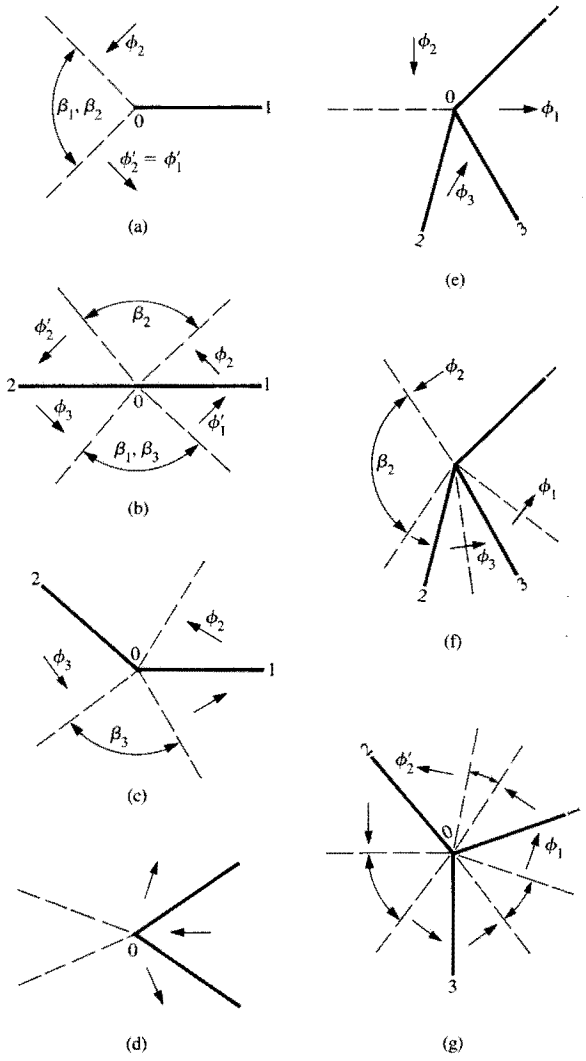


**Figure 18**

(a) The simplest free cluster. (b) A free doublet with two domain walls that are in line ($\alpha_1 = \alpha_2 - \pi$). (c) A free doublet with a kink in the domain walls at the cluster knot. (d) The tip of a zigzag wall. (e) A uniform subcluster in a free triplet. (f) A domain-wall configuration of Figure (18e) with only rotating domains. (g) Reconstruction of the free cluster of Figure 20.

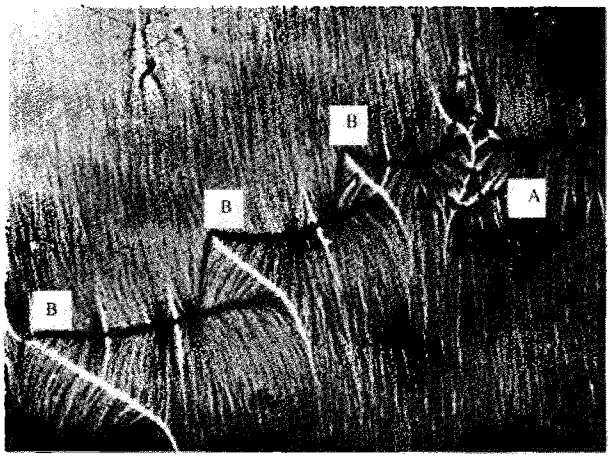


Figure 19

Lorentz image of free subclusters with uniform subclusters indicated by B and two pairs of nonlinked domain walls which potentially constitute the zigzag tips (courtesy of R.H. Wade [60]).

Figure 20

A ferrofluid pattern of a completely rotating free triplet with traces that show the presence of the rotation segments (Permalloy thickness 2500 Å).

The number of domain walls in the free clusters considered up to now has been too small to yield completely uniform free clusters, which according to our view should contain at least four domain walls. **Figure 22(a)** (due to Herd et al. [40]) shows four completely uniform free quartets. According to Equation (7),

$$\gamma_1^4 = (\alpha_4 - \alpha_3) + (\alpha_2 - \alpha_1)$$

is equal to $\pi$ for such a cluster. This type of pattern is frequently met in thin Permalloy films and is well known

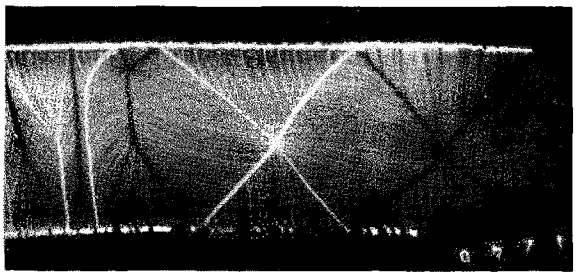

Figure 21

Lorentz image of several edge clusters of completely rotation- triplets and of two completely rotating free quartets (cour of S. R. Herd, IBM T. J. Watson Research Center, Yorkt Heights, NY).

as *cross-tie wall*. The Lorentz image due to Feldtkeller and Fuchs [65] [see **Figure 22(b)**] demonstrates the lar number of domain walls that can reveal themselves in one single (in this case free) cluster.

Let us recapitulate the most important properties of the free cluster as discussed above.

1. The sector angle of a specific domain of a cluster ca generally be decomposed into two uniform sectors adjacent to the domain walls and a rotation segmer in the middle—a rotating domain, or this angle contains one single uniform sector—a uniform domain.
2. The rotation sense of the rotation segments is the same in a specific free cluster.
3. The uniform subclusters consist of an even number larger than one of uniform domains, while no such restriction applies to the rotating subclusters.
4. A completely uniform cluster consists of an even number of domains and walls larger than three, wh an odd cluster contains at least one rotating domair
5. The clock sense of the domain walls alternates in a uniform (sub)cluster, while it is the same for all wal of a rotating (sub)cluster.

*The edge clusters*

The edge cluster is characterized by the location of its cluster knot at one of the edges of the object. In contra to the free clusters, any closed path around the edge- cluster knot contains a finite arc outside the magnetic medium, in which the previously signified rotation sectors and uniform sectors have no meaning. Therefo it should be expected that the general order in the edge clusters deviates from that in their pendant—the free clusters.

The location of the edge-cluster knot at the edge of t object has important implications for the correlation

between the **M** distributions in both outermost domains of the edge cluster. The **M** component normal to the edge must be continuous at the edge and thus across the cluster knot, in order to prevent discontinuities in the surface-charge density from occurring. Such a discontinuity should lead to a singularity in the tangential component of the total Maxwell field, which should cancel out the discontinuity, as can be seen from Equation (1). Because of the continuity in the normal component in **M**, a rather strong correlation exists between the magnetization directions in both outermost uniform sectors of the edge cluster. Two situations can be distinguished: first, the **M** components tangential to the edge in both outermost uniform sectors are parallel—the so-called odd edge clusters—or they are opposite, resulting in even edge clusters. It has been proved elsewhere [25, 66] that an odd edge cluster consists of an odd number of domain walls larger than two [10], while an even cluster with the opposite tangent **M** components at the edge contains an even number of domain walls larger than one. Moreover, it has been revealed [25] that the edge clusters merely contain uniform domains. This fact indicates that a close relationship exists between the mutual positions of the domain walls and the **M** distribution near the cluster knot. This inter-"waveness" is reflected by the following relation [25] for an edge cluster with $n$ walls (see **Figure 23**):

$$\phi_{i+1} = \frac{\pi}{2} - (-1)^{i+n}\gamma_1^n + 2\gamma_1^i - (-1)^i k\pi + k_i 2\pi, \qquad (10)$$

where $k_i = 0, \pm 1, \pm 2, \cdots$, with

$$\gamma_i^j = \sum_{h=i}^{j} (-1)^{j-h}\alpha_h,$$

if $j \geq i \geq 1$. If this condition is not satisfied, $\gamma_1^j = 0$.

The parameter $k$ is either zero or one, and is fixed for a specific edge cluster. It is obvious from Equation (10) that the **M** distribution, apart from a freedom of 180° represented by $k$, is uniquely specified by the mutual domain-wall positions. It is often convenient to have an explicit expression for the domain-wall angle $|\psi_i|$ of wall ($i$) at our disposal, which follows immediately from Equations (7b) and (10):

$$|\psi_i| = |\phi_{i+1} - \phi_i|$$
$$= 2|(-1)^{i+n}\gamma_{i+1}^n + \gamma_1^{i-1} + \pi 1_i| \qquad (11)$$

where $1_i$ is chosen such that $0 \leq |\psi_i| \leq \pi$.

Since the above formulas, though general, are a little obscure, they are made explicit in **Table 1** for a number of simple clusters which are frequently met in practice.

Within the present framework, the edge singlet, i.e., a single domain wall with an extremity at a smooth edge, is only possible when the domain wall touches at the edge.

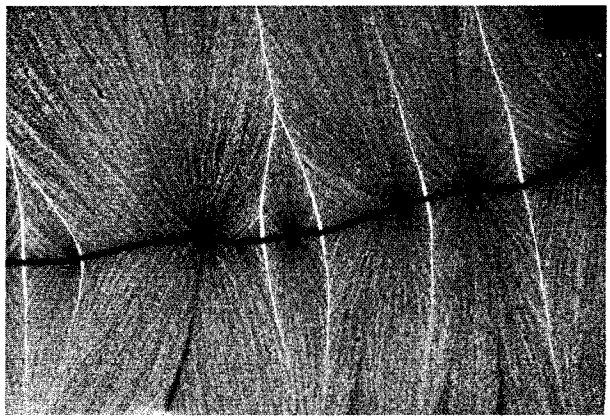

(a)

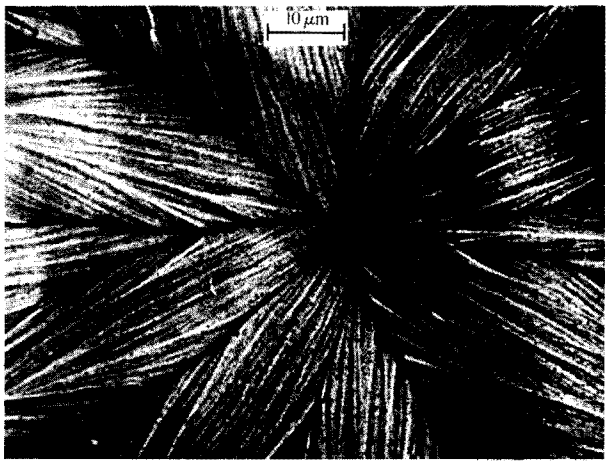


(b)

**Figure 22**

(a) Four completely uniform quartets in a 560-Å-thick Permalloy layer [40]. (b) A free sextet in a 300-Å-thick Permalloy layer [65].

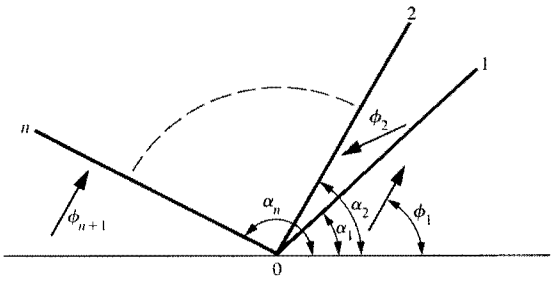


**Figure 23**

The mutual positions of the domain walls in an (odd) edge cluster and the **M** directions in the domains.

**Table 1** The magnetization directions $\phi_i$ and the wall angles $|\psi_i|$ for singlet, doublet, triplet, and quartet edge clusters.

| *Cluster type* | **M** *directions,* $\phi$ (*For* $\mathbf{M}' = -\mathbf{M}$; $\phi + \pi = \phi'$) | | *Wall angle,* $\psi_i$ $0 \leq \lvert\psi_i\rvert < \pi$ | |
|---|---|---|---|---|
| Singlet $n = 1$ | Possible only when wall touches edge | | | |
| Doublet $n = 2$ | $\phi_1 = \frac{\pi}{2} - (\alpha_2 - \alpha_1)$ | (12a) | $\lvert\psi_1\rvert = 2\,\lvert l_1\pi - \alpha_2\rvert$ | (12d) |
| | | | $l_1 = 1;\quad \alpha_2 \geq \frac{\pi}{2}$ | |
| | $\phi_2 = \frac{\pi}{2} + (\alpha_2 + \alpha_1)$ | (12b) | | |
| | | | $l_1 = 0;\quad \alpha_2 < \frac{\pi}{2}$ | |
| | $\phi_3 = \frac{\pi}{2} + (\alpha_2 - \alpha_1)$ | (12c) | $\lvert\psi_2\rvert = 2\,\lvert\alpha_1 - l_2\pi\rvert$ | (12e) |
| | | | $l_2 = 0;\quad \alpha_1 \leq \frac{\pi}{2}$ | |
| | | | $l_2 = 1;\quad \alpha_1 > \frac{\pi}{2}$ | |
| Triplet $n = 3$ | $\phi_1 = -\frac{\pi}{2} + \alpha_3 - (\alpha_2 - \alpha_1)$ | (13a) | $\lvert\psi_1\rvert = 2\,\lvert\alpha_3 - \alpha_2 + l_1\pi\rvert$ | (13e) |
| | | | $l_1 = 0;\quad (\alpha_3 - \alpha_2) \leq \frac{\pi}{2}$ | |
| | $\phi_2 = -\frac{\pi}{2} - \alpha_3 + (\alpha_2 + \alpha_1)$ | (13b) | | |
| | | | $l_1 = -1;\quad (\alpha_3 - \alpha_2) > \frac{\pi}{2}$ | |
| | $\phi_3 = -\frac{\pi}{2} + \alpha_3 + (\alpha_2 - \alpha_1)$ | (13c) | | |
| | $\phi_4 = -\frac{\pi}{2} + \alpha_3 - (\alpha_2 - \alpha_1)$ | (13d) | $\lvert\psi_2\rvert = 2\,\lvert\alpha_3 - \alpha_1 + l_2\pi\rvert$ | (13f) |
| | | | $l_2 = 0;\quad (\alpha_3 - \alpha_1) \leq \frac{\pi}{2}$ | |
| | | | $l_2 = -1;\quad (\alpha_3 - \alpha_1) > \frac{\pi}{2}$ | |
| | | | $\lvert\psi_3\rvert = 2\,\lvert(\alpha_2 - \alpha_1) + l_3\pi\rvert$ | (13g) |
| | | | $l_3 = 0;\quad (\alpha_2 - \alpha_1) \leq \frac{\pi}{2}$ | |
| | | | $l_3 = -1;\quad (\alpha_2 - \alpha_1) > \frac{\pi}{2}$ | |
| Quartet $n = 4$ | $\phi_1 = \frac{\pi}{2} - (\alpha_4 - \alpha_3) - (\alpha_2 - \alpha_1)$ | (14a) | $\lvert\psi_1\rvert = 2\,\lvert\alpha_4 - \alpha_3 + \alpha_2 + l_1\pi\rvert$ | (14f) |
| | | | $\lvert\psi_2\rvert = 2\,\lvert\alpha_4 - \alpha_3 + \alpha_1 + l_2\pi\rvert$ | (14g) |
| | $\phi_2 = \frac{\pi}{2} + (\alpha_4 - \alpha_3) + (\alpha_2 + \alpha_1)$ | (14b) | $\lvert\psi_3\rvert = 2\,\lvert\alpha_4 - \alpha_2 + \alpha_1 + l_3\pi\rvert$ | (14h) |
| | | | $\lvert\psi_4\rvert = 2\,\lvert\alpha_3 - \alpha_2 + \alpha_1 + l_4\pi\rvert$ | (14i) |
| | $\phi_3 = \frac{\pi}{2} - (\alpha_4 - \alpha_3 + (\alpha_2 - \alpha_1)$ | (14c) | | |
| | $\phi_4 = \frac{\pi}{2} + (\alpha_4 + \alpha_3) - (\alpha_2 - \alpha_1)$ | (14d) | | |
| | $\phi_5 = \frac{\pi}{2} + (\alpha_4 - \alpha_3) + (\alpha_2 - \alpha_1)$ | (14e) | | |

The reason for this can easily be understood. A domain wall is characterized by a finite jump in **M**—the average lateral component $\langle \mathbf{M} \rangle$ parallel to the film plane—across the wall surface. It can easily be seen (**Figure 24**) that the

M directions at opposite sides of the wall are related by

$$\phi_2 = \pi - \phi_1 + 2\alpha_1 + k\pi. \quad (15)$$

The M component normal to the edge must be continuous across the knot; i.e., $\cos \phi_1 = \cos \phi_2$ in order to prevent a surface-charge discontinuity. From Equation (15), it follows that this condition is satisfied only when $\phi_1 = \alpha_1 \pm \pi/2$, i.e., when the wall angle reduces to zero at the edge, or when the wall touches at the edge. Thus, an isolated distinctive domain wall with extremities at the edges points to an acute edge deformation or to a lack in the resolution power, so that satellite walls remain undetected, or to a relatively large domain-wall core width, so that the discontinuous character vanishes, and, finally, to a three-dimensional domain configuration.

In practice, edge doublets such as those shown in **Figure 25(a)** are frequently encountered. Note that the clock senses of the walls are opposite in the Lorentz image. This should be expected, since the edge clusters consist merely of uniform domains. At low external fields, the magnetization tends to be parallel to the edge $\phi_1 \simeq 0$ or $\pi$, so that the angle between the walls should be about $\pi/2$ [see Equation (12a)], which is in compliance with the images discussed above. Observe that, apart from the uncertainty of $\pi$, only the angle $(\alpha_1 - \alpha_2)$ determines the M directions in the outermost domains of the edge doublet [see **Figures 25(b)** and **25(c)**]. Consider a degenerated doublet of which one wall, e.g., wall (1), touches the edge at 0. From Equation (12e), it is seen that the wall angle reduces to zero; i.e., the doublet has been converted into the only possible singlet. This degenerated doublet state is of great significance for the doublet creation, as we shall see.

The edge triplets in the Lorentz image of Figure 21 also exhibit the alternating pattern of black and white domain walls. Note that the middlemost domain walls are most visible; this has also been observed in numerous images of the edge triplet by means of the ferrofluid technique. Equation (13) provides an explanation. In the next section, we demonstrate that all of the walls of the edge triplets tend to develop themselves along the same line—the so-called creation line—and the angle $(\alpha_1 - \alpha_2)$ is relatively small, so that $1_1$, $1_2$, and $1_3$ are zero in Equations (13e–g). It is obvious that the wall angle $|\psi_2|$, being $2(\alpha_2 - \alpha_1)$, is equal to the sum of $|\psi_1|$ and $|\psi_3|$. Therefore, under the assumption that all walls possess the same type of structure, the visibility of this middlemost wall is the best. Again, from Equations (13e–g), it is readily understood that deviations from this trend are expected when the domain-wall angles become large. Consider the degenerated triplet in which two, e.g., walls (1) and (2), of the three walls coincide. From Equation (13g), it follows that the angle of wall (3) is zero and that the M distribution resembles a continuous configuration

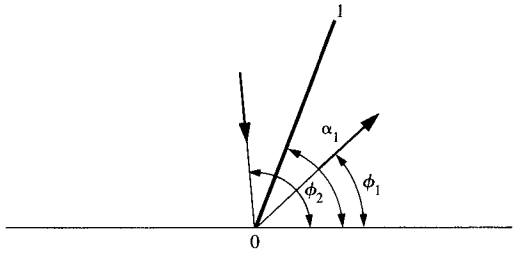


**Figure 24**

An edge singlet.

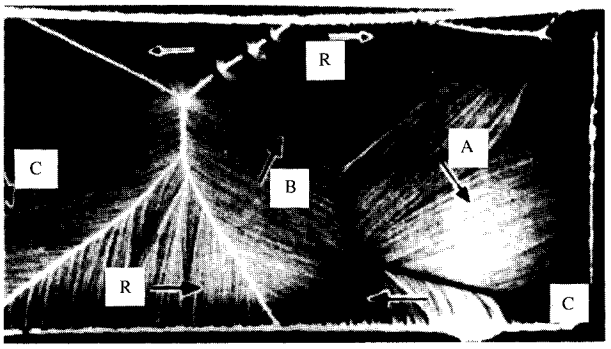


(a)

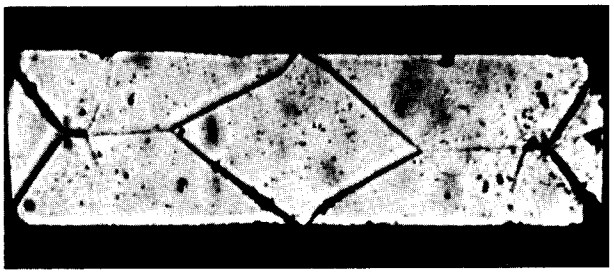

(b)

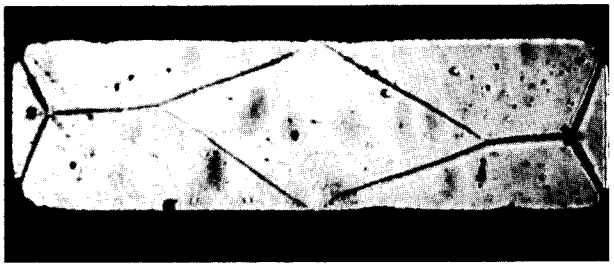

(c)

**Figure 25**

(a) Several edge doublets in a 600-Å-thick Permalloy layer [62]. (b, c) The angle $\alpha_1 - \alpha_2$ between the doublet wall as a function of the field $\mathbf{H}_0$ perpendicular to the long edge, i.e., as a function of $\phi_1$. Permalloy (60 × 20 $\mu$m, thickness 2500 Å).

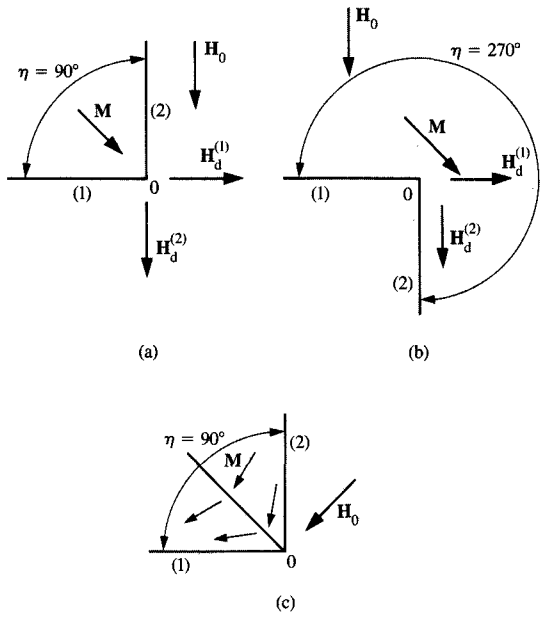


**Figure 26**

The **M** distributions near corners: (a) An acute corner; $\eta = 90°$. (b) An obtuse corner; $\eta = 270°$. (c) The acute corner of (a) with $\mathbf{H}_0$ rotated 45°.

when the infinitesimally small sector between walls (1) and (2) is ignored. Consider the triplet of which all the walls coincide. All wall angles reduce to zero [see Equations (13e–g)], and a continuous **M** state results. This extreme situation will turn out to be of great significance to the creation of the edge triplets.

The main characteristics of the edge clusters can be condensed into the following statements:

1. The edge clusters are completely uniform clusters, in which the clock senses of the walls alternate consecutively when tracing the cluster in a clockwise or counterclockwise direction.
2. Apart from an uncertainty of 180° in the **M** directions, a one-to-one correspondence exists between the mutual wall positions and the **M** distribution of the cluster.
3. The **M** components tangential to the edge in the outermost domains are parallel in an odd edge cluster and are opposite in an even edge cluster.

*The corner clusters*

In corner clusters, the cluster knot is situated at an object corner, at which, in principle, the normal to the edge performs a discontinuous direction change. The acuity of the actual corner is of decisive significance to the properties of the **M** distribution. When the corners are rounded off, the "corner" cluster behaves as a hybrid of a corner, edge, and/or free clusters [25]. For that reason, the general relations for the corner clusters have a smaller practical scope than that of the previously discussed cluster relations.

One of the peculiarities in the **M** distribution near the corners is the occurrence of persistent magnetized states. Because this subject was discussed extensively in [25], we confine ourselves to a brief outline only. Let us consider an acute corner, say with corner angle $\eta = 90°$ [see **Figure 26(a)**]. An external field $\mathbf{H}_0$ is applied, which forces **M** to have a component normal to edge (1) near the corner. However, at the corner, the surface-charge density due to this normal **M** component diminishes and a singularity in the field component parallel to the edge under discussion arises. At first glance, the enormous strength of this field should force **M** to orient itself parallel to edge (1); however, a normal **M** component at the other corner edge (2) will develop itself in that case. Note that the signs of the charges at both edges that tend to arise are equal, so that the total field is oriented as indicated in Figure 26(a). In the stable configuration, the magnetization near the far corner is directed parallel to the bisector of both edges (1) and (2). Note that the role of the demagnetizing fields has been converted from a force that tends to a situation with zero mean object magnetization into a force that, at least locally, creates a magnetized state which appears to be rather persistent. These "locked" regions, in which the demagnetizing fields are magnetizing, have a significant impact on the hysteresis of the soft-magnetic objects. In such a region, only the domain walls that coincide with one or both edges can occur in the ideally soft-magnetic media [24].

The situation in an obtuse corner is slightly different [see **Figure 26(b)**]. Again, the external field $\mathbf{H}_0$ forces **M** to create a positive charge at edge (1). However, this time, the charge at edge (2) has the opposite sign, and the ultimate **M** direction near the far corner is perpendicular to the bisector of both edges. In light of the above discussion, the significance of the acuity of the corner is obvious and needs no further comment. It should be discerned that the charge collected at the top and bottom surfaces of the film near the corners may have a significant contribution to the field distribution in the corner region when the rounding radius is too large compared to the film thickness. In this situation deviations, particularly in the acute corner, occur with respect to the **M** directions predicted above.

The foregoing arguments tend to lead to the conclusion that the corner clusters in perfect objects should only be present when the external field is zero. This is not always true, as can be deduced from **Figure 26(c)**, in which the

external field $\mathbf{H}_0$ is rotated over 45° with respect to Figure 26(a). In this case, a vanishingly small magnetic surface-charge density suffices in the corner to compensate $\mathbf{H}_0$. Away from the vertex, a finite surface charge takes care of this compensation. As a consequence, domain walls, i.e., corner clusters, can be located in such a corner region.

The above discussion indicates that the magnetization in the outermost uniform sectors of a corner cluster is parallel to the corner edges. It has been proved elsewhere [25] that the clusters in the acute corners (i.e., with corner angle $\eta < \pi$) are always completely uniform and satisfy

$$\gamma_1^n = \frac{\eta}{2}, \tag{16}$$

where $n$ is the number of domain walls and $\gamma_1^n$ is given by Equation (7b). In an obtuse corner with $\eta > \pi$, rotation segments may occur in the corner sector that is 90° apart from both edges. The completely uniform clusters in these obtuse corners satisfy Equation (16). Moreover, it can be shown that any completely uniform corner cluster in which the **M** vectors in the exterior domains are either both pointing toward the cluster knot or both away from the knot contains an even number of domain walls. A completely uniform corner cluster with an odd number of domain walls has an **M** vector pointing toward 0 and one pointing away from 0 in both exterior domains. A number of examples of completely uniform corner clusters in Permalloy elements are presented in **Figure 27**. A reasonable agreement with Equation (16) is found. **Figure 28** shows Lorentz images due to Gondo et al. [67], where the corners are magnetically saturated.

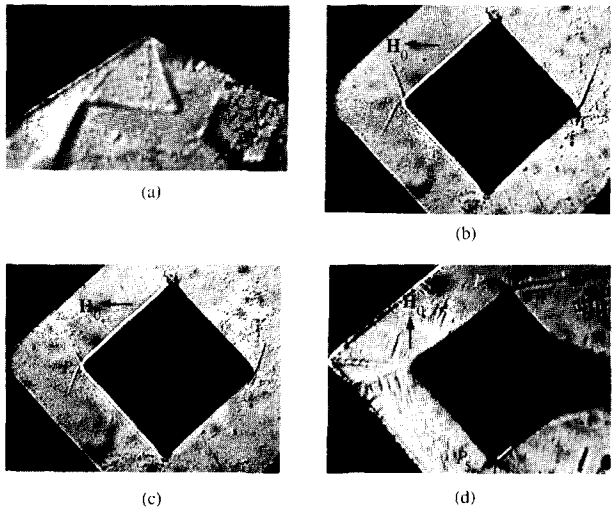


Figure 27

(a) A completely uniform doublet; $\mathbf{H}_0$ = 260 A/m (= 3.3 Oe). $\eta$ = 124°; $\gamma_1^2 = \alpha_2 - \alpha_1$ = 67°. (b) A completely uniform doublet at $P$; $\mathbf{H}_0$ = 1280 A/m (= 16 Oe). $\eta$ equals 270°; $\gamma_1^2 = \alpha_2 - \alpha_1$ = 139°. (c) A completely uniform doublet at $P$; $\mathbf{H}_0$ = 2400 A/m (= 30 Oe). $\eta$ = 270°; $\gamma_1^2$ = 130°. (d) A completely uniform triplet; $\mathbf{H}_0$ = 2500 A/m (= 31 Oe). $P_3$, $\eta$ = 266°, $\gamma_1^3$ = 137°; $P_5$, $\eta$ = 266°, $\gamma_1^3$ = 132°.

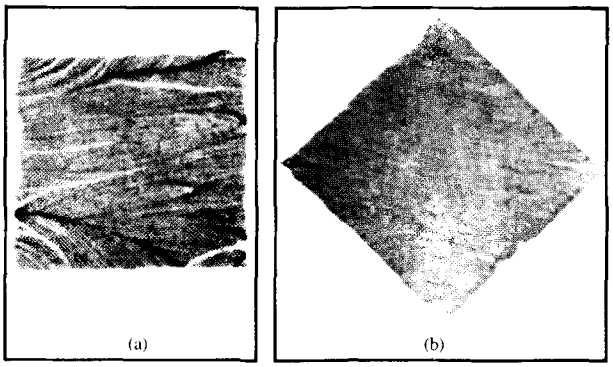


Figure 28

Lorentz micrographs of a Permalloy thin film (92 × 92 $\mu$m, 500 Å thick) [67]. External field: (a) 400 A/m (= 5 Oe); (b) 1200 A/m (= 15 Oe).

• *Domain-wall clusters: Reversible transformations*

In the previous section, we have covered the correlation between the mutual positions of the domain walls in the clusters and the **M** distribution near the cluster knot in the domains. Two **M** modes, namely the uniform sector and the rotation segment, can be distinguished. The location of the cluster knot with respect to the edges of a thin-film element determines the combination of uniform sectors and rotation segments that can occur in a specific cluster. This connection emerges very distinctly in the edge clusters, which lack the rotation segments.

Domain structures can be considered as concatenations of domain-wall clusters. Clusters are added to and/or removed from the domain structure during its development phase. How the various clusters can transform and join an already existing domain configuration is discussed in this section.

The conversions in the **M** distribution are known to bear a reversible character within finite ranges of the external field as long as its time rate of change is sufficiently small. This only applies when the impact of structural defects, which may particularly hinder the motion of the domain walls and the cluster knots, is negligible. The subordinate role of the imperfections is one of the prerequisites that must be met by the soft-magnetic media which are the subject of this paper. At the boundaries of the above reversible ranges, an

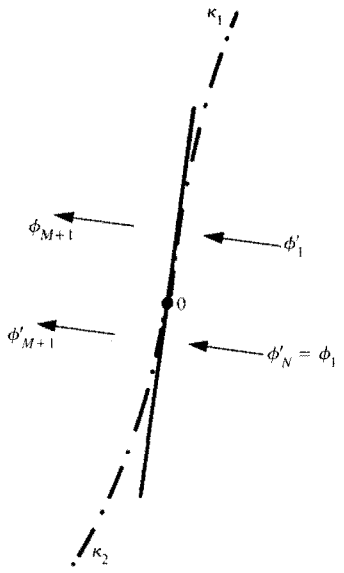


**Figure 29**

The locally uniform state with two creation lines at either side of the cluster knot.

instability in the magnetization structure heralds a short period of agitated spin motion, during which energy is dissipated. In contradiction to this, the conversions in the reversible ranges take place via a continuous sequence of equilibrium states, in which the dipoles in the entire object are in stable equilibrium in each intermediate stage. In this section, we confine ourselves to such reversible transformations.

In general, the magnetization conversions take place by a coherent movement of domain walls and by a simultaneous rotation of the dipoles in the domains. The domain structure develops by concatenating domain-wall clusters. One possible reversible manner of adding clusters can be summarized as follows. Those clusters that do not have all of their domain walls connected to other clusters may initiate the creation of new clusters which are then annexed to the domain structure. The addition of a novel cluster requires the formation of new domain walls of finite length. The dipoles within and adjacent to this domain wall must suddenly rotate over a finite angle, when the wall angle of such a novel domain wall is finite in the earliest phase of its existence. This process must be attended by energy losses in order for the precession of the dipoles to die out. Therefore, the wall angle(s) of a domain wall(s) with a finite length(s) should be zero during the incipient phase of a reversible process. Of course, its pendant—the vanishing of a domain wall—should take place by a gradual decline to zero of the domain-wall angle. We refer to the former reversible process, in which domain walls are added, as (sub)cluster creation, and to the latter as cluster fading. Their irreversible counterparts are called (sub)cluster nucleation and annihilation, respectively.

Apart from (sub)cluster creation, one other reversible process—so-called cluster furcation—exists by which the number of clusters can be increased. In principle, the wall angle(s) of the newly created domain wall(s) are finite from the very beginning, while the wall length(s) grow(s) from zero in the incipient phase to a finite value, so that a jumpwise alteration in the **M** distribution only takes place in an infinitesimally small volume. As a consequence, no energy barricade is raised against this process. Upon cluster furcation, the cluster knot of an already existing cluster is split up into two or more knots. These knots are generally interconnected by one or more intermediate domain walls. The length(s) of these newly formed intermediate domain wall(s) increase(s) from zero in the beginning to a finite value. The above cluster furcation has its pendant in the cluster fusion, at which two or more cluster knots amalgamate in a reversible fashion.

Both categories of reversible cluster processes are closely examined in the two following sections. An exhaustive treatment is not pursued; rather, the various possibilities are elucidated by means of a restricted number of frequently occurring conversions.

*(Sub)cluster creation and fading*

As discussed, the wall angle(s) of the newly added domain walls are zero during the incipient phase of (sub)cluster creation. The gradual growth of these wall angles during their development from zero implies that each domain wall should initially coincide with an orthogonal trajectory of the original continuous **M** vector field through the (prospective) cluster knot. A strong coherence between the domain walls has to be expected when the domain walls of the new (sub)cluster coincide with the same trajectory, which we call the creation line of the (sub)cluster. It is obvious that the wall angle of each domain wall along this creation is zero at the beginning. Further discussion is focused completely on the creation process, because the cluster fading is a duplicate of the cluster creation which progresses in just the opposite direction.

Consider the creation of a free cluster with a prospective cluster knot 0 in a region of continuous local uniform magnetization (see **Figure 29**). Two creation lines at either side of 0, indicated by $\kappa_1$ and $\kappa_2$, offer the

possibility of subcluster creation. First, we assume that the creation process confines itself to one side, say along $\kappa_1$. Note that $\phi_1$ and $\phi'_{M+1}$ remain parallel, so that the subcluster along $\kappa_1$ bears close resemblance to the odd edge cluster; i.e., it merely consists of uniform domains between an odd number of domain walls. It can be shown [25] that at least one of the two subclusters is of the uniform type, containing an odd number of domain walls, while a rotation segment may be present in its counterpart. A rotation segment contains an infinite number of potential creation lines along which new subclusters can develop themselves. No such creation lines are found in the uniform domains and, as a consequence, a completely uniform cluster should be transformed into a cluster with a rotating subcluster before the number of walls can be changed. Let us proceed to the edge clusters.

It has been discussed in the subsection on edge clusters that the edge clusters merely consist of uniform domains, and as a consequence no subcluster can be added or removed in a reversible fashion. With this, the subject of the modification of the edge cluster seems to be terminated. However, do not forget the creation of a complete edge cluster. In **Figure 30(a)**, the creation line with prospective cluster knot 0 is depicted in a region adjacent to the edge with continuous magnetization. In principle, an edge cluster can be created. Note that the **M** in both prospective exterior domains has to be parallel. According to the subsection on edge clusters, an edge cluster can only have an odd number of domain walls. An edge singlet is impossible because the creation line is not parallel to the edge in Figures 30(a) and **30(b)**. Consider the creation of an edge triplet in detail. A slight change in the external field forces the triplet to unfold, at which the domain walls start to rotate about the cluster knot 0. Simultaneously, the wall angles gradually increase from zero to a finite value. According to Equations (13e–g), the wall angle of the middlemost wall is always the largest in this phase, and, in general, its visibility is the best. Depending on the observation technique, it might occur that only the middlemost wall can be resolved in the incipient phase of the creation, so that the impression of an edge singlet might develop. How about the even edge clusters?

Because of the uniformity of the domains in the odd edge cluster, the even edge clusters cannot develop themselves from the normal odd edge clusters by a subcluster creation process. The degenerated configuration with one single domain wall that touches the edge at the prospective doublet knot 0 constitutes the only alternative [see the subsection on edge clusters and **Figures 30(c)** and **30(d)**]. Note that a creation line is present along which uniform subclusters can develop. In view of the original continuity of the **M** distribution near the creation line, the number of domain walls in the subcluster is odd [compare Equations (13d) and (14e) or (12c)]. In other words, an even edge cluster can be created. This time, the uniform subcluster may consist of one single domain wall. In order to enforce this wall, the touching domain wall must rotate around knot 0, and the wall angle of wall (1) increases in compliance with Equation (12d) [see Figure 30(d)].

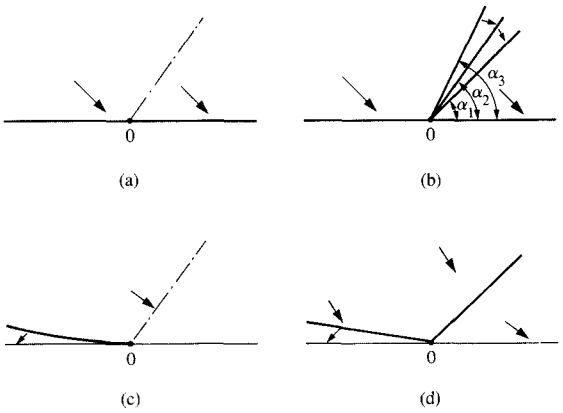


**Figure 30**

The creation of (a, b) an odd edge cluster; (c, d) an even edge cluster.

Both of the edge cluster creation processes discussed above are very frequently observed, and a number of examples are reviewed in the course of this paper.

*Cluster furcation and fusion*

In the previous section, it was emphasized that the creation of (sub)clusters is often impossible because of the absence of adequate creation lines, as for example in the edge and the corner clusters. The cluster furcation constitutes an alternative by which the required domain-structure transformations can yet take place.

During cluster furcation, a cluster knot is split into two or more knots, which are connected by (an) intermediate domain wall(s) which have zero length during the incipient phase. The directions of these early walls are determined by the **M** distribution near the original knot just prior to its furcation. Of course, the actual cluster knot possesses finite dimensions, so that a finite field change is required to separate the knots and to let the intermediate domain walls arise. As a result, the course of these walls will deviate slightly from that derived from the somewhat simplified view of the **M** distribution in this study.

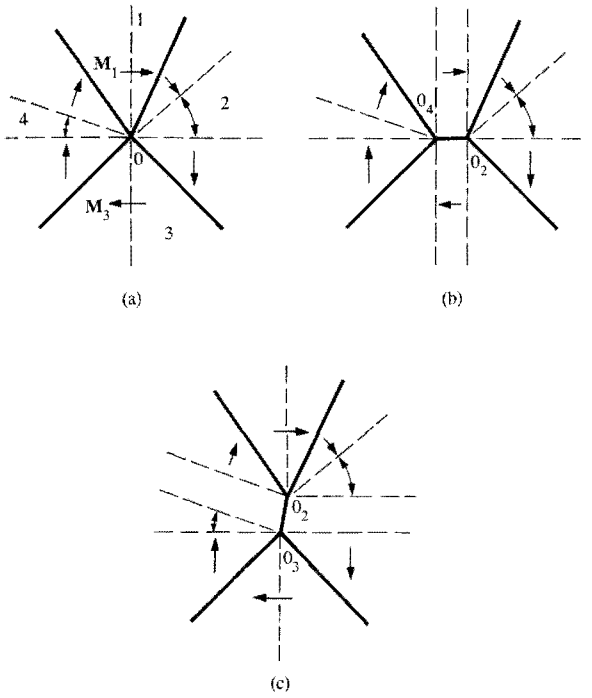


(a) A completely rotating free quartet. (b, c) The furcation of the completely rotating quartet into two free triplets.

Another feature of cluster furcation is closely interwoven with the internal structure of the cluster knots. The dipole configuration in the knot is closely bound up with the number of interconnected domain walls and their structures, the **M** distribution in the continuous regions near the knot, the film thickness, the magnetic history, etc. Therefore, it may happen that the knot structures have to bear a completely different character before and after the furcation. It is certainly not evident that the transformations of the original cluster knots can take place without overcoming energy thresholds. Such transformations, when not blocked, are attended by energy losses and are irreversible. Here, we ignore these aspects of the internal structure transformation of knots and focus on the global relationship between the mutual orientation of the walls and the **M** distribution near the knots. Again, we confine ourselves to the presentation of a few illustrative examples. Further information can be found in [25].

As already stated, the orientation of the newly formed intermediate domain wall is determined by the **M** distribution just prior to the furcation. We make this statement explicit by considering the furcation of a completely rotating free quartet [see **Figure 31(a)**] into two free triplets. One of the two possible realizations is presented in **Figure 31(b)**. The intermediate domain wall between $0_2$ and $0_4$ cannot carry a net charge, so it is directed along the normal to the bisector of both magnetization directions $\mathbf{M}_1$ and $\mathbf{M}_3$. This wall direction is uniquely determined when the domains separated by the intermediate wall are uniformly magnetized. (Note that a uniform domain is always uniformly magnetized; however, a uniformly magnetized domain might also be of the rotating type.) A greater flexibility exists for the furcation mode of **Figure 31(c)**, because each combination of a magnetization direction from the rotation segment in domain 2 with a corresponding one from the rotation segment in domain 4 yields a potential direction of the intermediate wall. **Figure 32** provides an example of such a cluster furcation in a Permalloy element.

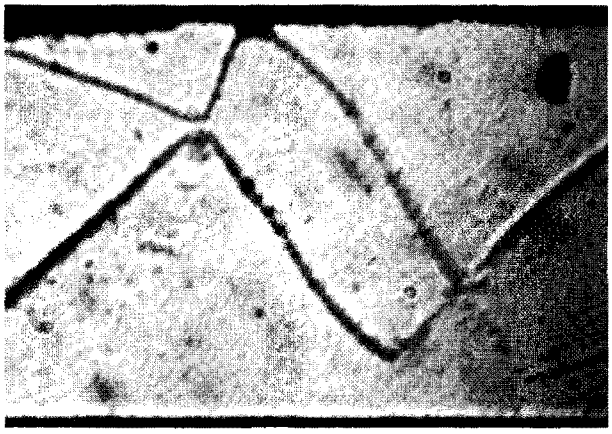

(a)

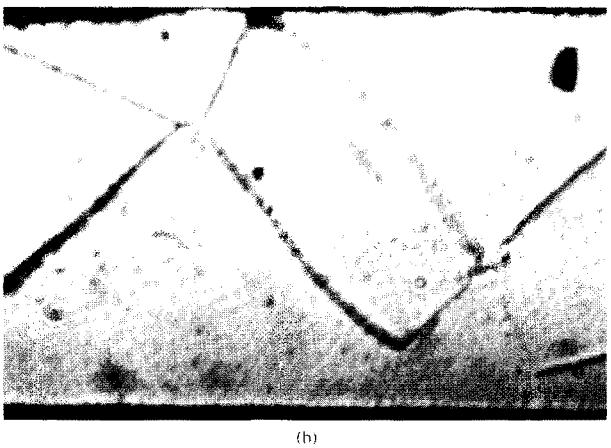

(b)

A cluster furcation corresponding to Figure 31(b) in a Permalloy element (a) before furcation; (b) after furcation.

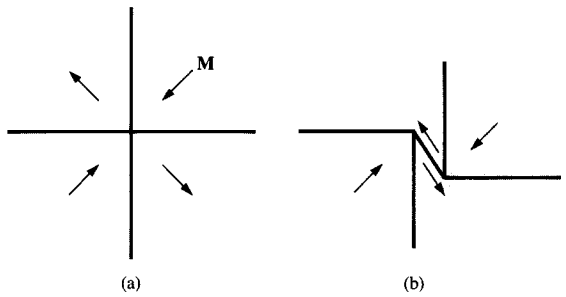


Figure 33

(a) A completely uniform quartet. (b) A possible furcation of the quartet of (a).

Let us focus on a completely uniform free quartet. A possible furcation is presented in **Figures 33(a)** and **33(b)**. More frequently, the transition of the quartet knot into four knots is observed. Such a transformation in a Permalloy element is presented in **Figure 34**. The complexity of this furcation likely originates in a conversion in the internal wall structure when the wall angles of two of the quartet walls grow beyond a certain critical angle at which a Bloch-type structure has a lower energy than the original Néel wall.

Another frequently observed cluster conversion is illustrated in **Figure 35**, which shows a rare example of a sequence of Lorentz images of a cluster conversion. This cross-tie wall can be regarded as a periodic pattern of the combination of a completely uniform free quartet and of a free doublet with two rotation segments [69]. As far as we can see, the direction of the intermediate domain wall is defined by the zero wall charge principle. The "wings" of the quartet gradually decrease in length upon the approach of the knots. Note that the wings become bowed when the symmetry of the locations of the doublet knots with respect to the quartet knot is removed. These curved wings separate the rotation segments from the uniform environments, so that the area occupied by the rotation segments gradually reduces to zero. Ultimately, the free quartet and doublet transform into a degenerated free doublet with two degenerated rotation segments, i.e., a continuous Néel wall. The inverse advance is demonstrated in **Figure 36**. A 180° Néel wall in a Permalloy element is moved through a defect, which reveals itself by a little ferrofluid cloud [see arrow in Figure 36(a)]. Upon passing, a pair of clusters is generated. The one at the left must be the completely

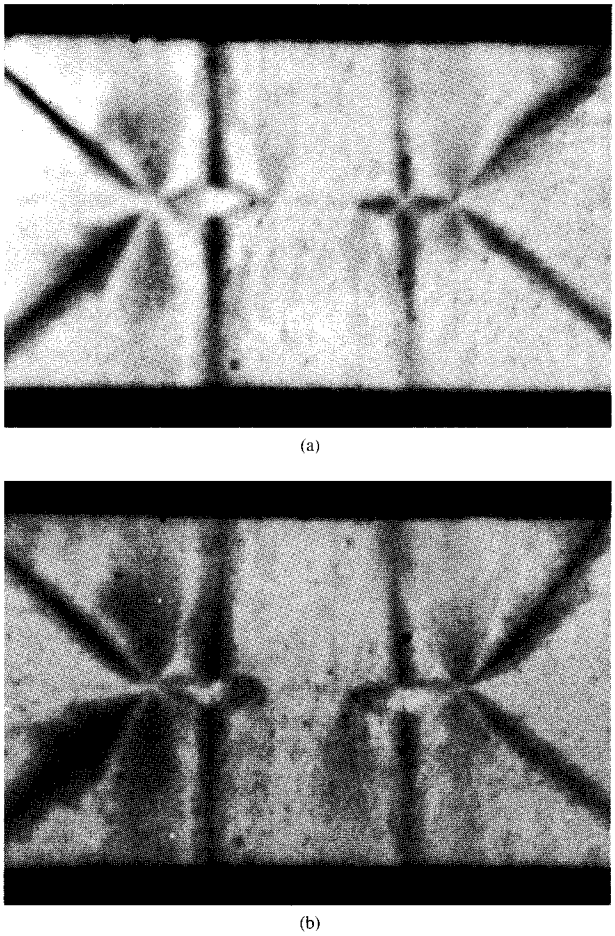


Figure 34

The furcation of a quartet into two quartets and two triplets: (a, c) the quartet and its **M** distribution near the knot; (b, d) the situation after the furcation.

uniform quartet, while its counterpart is a free doublet, i.e., a Bloch line. Note that the quartet's domain wall at the object-edge side betrays itself by a broadened cloud of ferrofluid, which is apparently a consequence of the

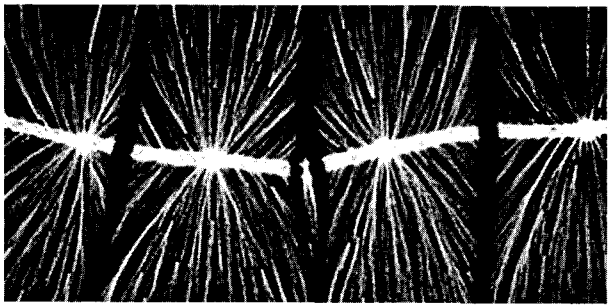

(a)

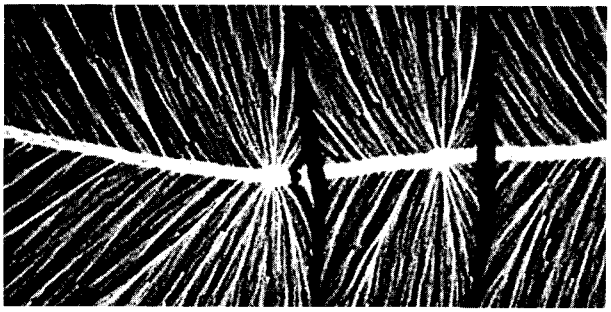

(b)

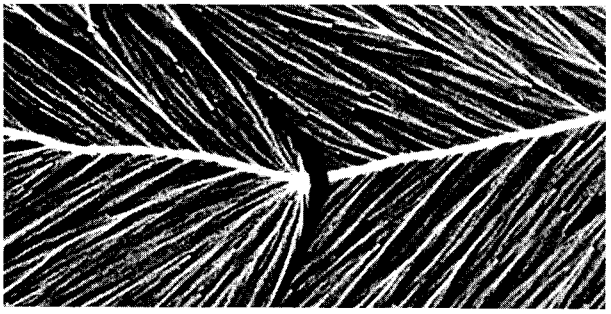

(c)

**Figure 35**

Lorentz pictures of the fusion of a free doublet and a completely uniform free quartet into a degenerate doublet, i.e., a Néel wall (courtesy of S. Middelhoek [68]).

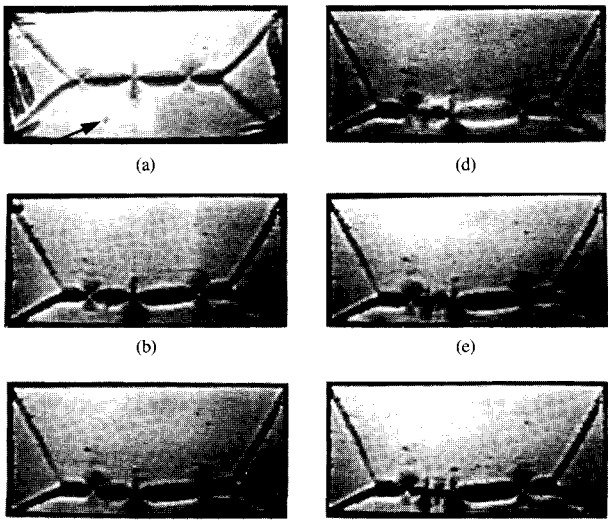

(a) (d) (b) (e) (c) (f)

**Figure 36**

The generation of a completely uniform quartet and free doublet pair by passing through a defect; Permalloy (60 × 30 $\mu$m, thickness 700 Å).

mismatch of a stepwise-changing **M** pattern near a wall and the requirement of the continuity of the surface charge at the edge.

The above examples of free quartet conversions provide an impression of the enormous variety in the furcations. Let us treat one final example of a frequently occurring process, namely an edge-triplet furcation into two edge doublets (see **Figure 37**). The change in the orientations of the old domain walls of Figure 37(a) is negligible during the furcation, so that the angles $\alpha_1$, $\alpha_2$, and $\alpha_3$ in Figures 37(a) and 37(b) may be considered equal. From Equations (12a) and (13a), it follows that $\alpha_4 = \alpha_3 - \alpha_2 + 2\alpha_1$. Even so, the doublet-wall orientation $\alpha_5$ in Figure 37(b) is equal to $2\alpha_3 - \alpha_2 + \alpha_1 - \pi$ by virtue of Equations (12c) and (13d). In other words, this furcation process can be completely described in terms of the cluster relations. An example of this edge-triplet splitting is presented in Figures 37(c) and 37(d). Note that the exterior walls of the triplet are difficult to see in the ferrofluid image, a fact that has been previously noted.

## 4. Reversible and irreversible domain transformations viewed from the perspective of wall clusters

In Section 3, we were occupied with the local coherence between the mutual domain-wall positions and its repercussions on the **M** distribution near the cluster knots. We have unveiled a high degree of order in these clusters and have shown that the number of domains in such clusters can be adapted by only two kinds of reversible processes, to wit (sub)cluster creation (fading) and cluster furcation (fusion). During this discussion we have dealt only with the geometrical aspects of the wall clusters and their transformations. No attention was paid to the question of how or why a particular cluster comes into being. This omission is considered in this section.

It has already been emphasized several times that any domain structure can be conceived as a concatenation of domain-wall clusters. During the development of a

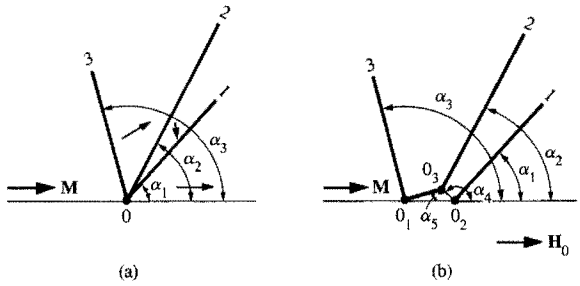


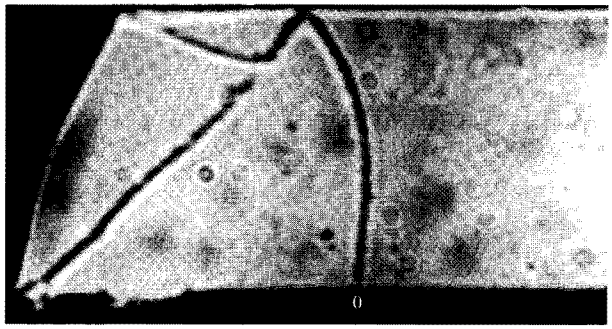


(c)

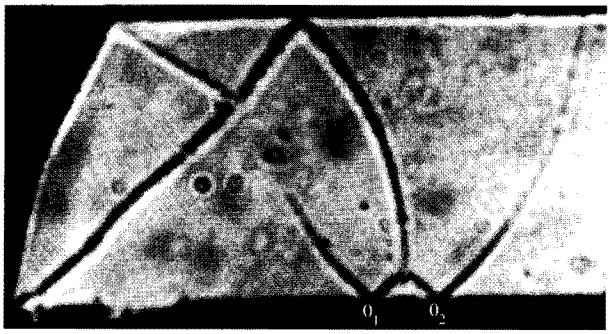


(d)

**Figure 37**

The furcation of an edge triplet into two edge doublets and a free triplet: (a, b) edge-triplet splitting; (c) $\mathbf{H}_0$ = 640 A/m (= 8.0 Oe); (d) $\mathbf{H}_0$ = 460 A/m (= 5.8 Oe).

(a)

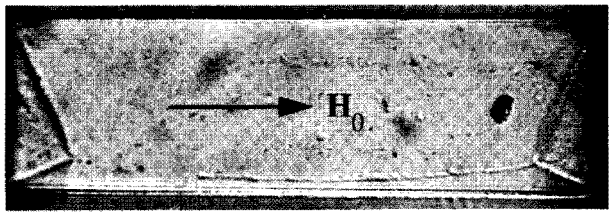


(b)

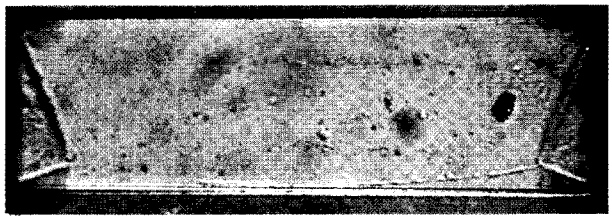

(c)

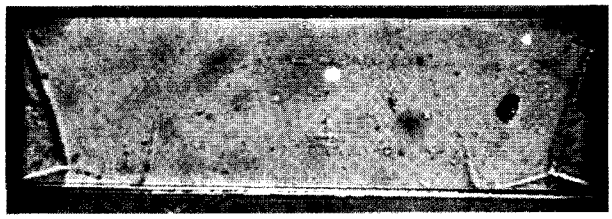

(d)

**Figure 38**

Domain conversions in a rectangular Permalloy specimen due to a uniform in-plane external field $\mathbf{H}_0$ parallel to the longitudinal (long) sample axis which increases from zero in (a) to $\mathbf{H}_0^{max}$ in (d). Permalloy (60 × 20 $\mu$m, thickness 2500 Å).

domain structure, domain-wall clusters are added to and removed from the domain structure. These alterations may take place in either a reversible or irreversible fashion, so that wall clusters, being a static concept, seem only to be relevant to part of the domain conversions, i.e., to the reversible ones. However, this will appear not to be the case. Indeed, the meaning of the wall-cluster concept is most apparent when the conversions at the reversible branches of the hysteresis loop are investigated. A high degree of order appears to characterize the domain-structure progression at the reversible branches, which can easily be comprehended in terms of cluster-creation processes. On the other hand, this concept also provides a tool for the analysis of the **M** distribution just before and just after an irreversible transformation, and allows us to trace the wall constellations that initiate such a conversion.

When an external field is applied along the longitudinal axis (**Figure 38**), the 180° wall moves toward the edge of the sample, while small jumpwise displacements due to the interference of defects can be detected. However, notwithstanding these defects, this

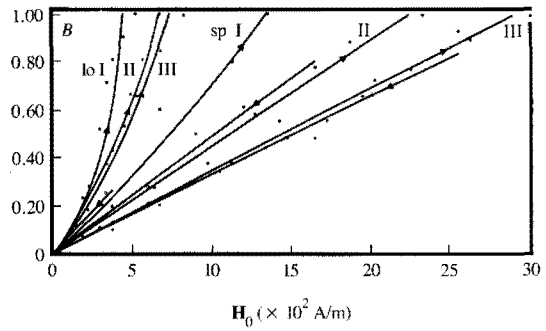


**Figure 39**

The position $B$ of the center of the 180° domain wall with respect to the central longitudinal symmetry axis of the sample as a function of $\mathbf{H}_0$; $\mathbf{H}_0$ is parallel to this symmetry axis. $B = 0$ corresponds to the position of the longitudinal symmetry axis at $\mathbf{H}_0 = 0$, i.e., at the midpoint of the sample width; $B = 1$ indicates that the wall is at the long edge of the specimen. Sputtered samples (sp) 2500 Å thick; lift-off samples (lo) 700 Å thick. Lateral dimensions: (I) 60 × 10 μm, (II) 60 × 20 μm, and (III) 60 × 30 μm.

**Table 2** The field strengths $\mathbf{H}_0^{ir1}$ and $\mathbf{H}_0^{ir2}$ as a function of the lateral dimensions and the thickness of the Permalloy specimens.

| *Sputtered samples (2500 Å)* | | | *Lift-off samples (700 Å)* | |
|---|---|---|---|---|
| *Size* (μm) | $\mathbf{H}_0^{ir1}$ (A/m) | $\mathbf{H}_0^{ir2}$ (A/m) | *Size* (μm) | $\mathbf{H}_0^{ir1}$ (A/m) |
| 60 × 30 | 3050 | 2590 | 60 × 30 | 835 |
| 60 × 20 | 2360 | 1675 | 60 × 20 | 685 |
| 60 × 10 | 1370 | 380 | 60 × 10 | 535 |

movement is basically reversible, as can be concluded from **Figure 39**, where the relative position $B$ of the 180° domain wall's midpoint with respect to the longitudinal sample axis is displayed as a function of $\mathbf{H}_0$ for Permalloy samples (83 Ni 17 Fe) with various lateral dimensions and thicknesses and manufactured by both sputter etching and the lift-off technique. For both categories, the wall displacement can be understood in terms of magnetostatic fields, which dominate the torque equilibrium of the dipoles.

We descend a little deeper into the magnetostatic aspects of the above domain-wall displacement which terminates at the field $\mathbf{H}_0^{ir1}$ when the center of the wall touches the edge. First of all, we want to explain the dependence of the $\mathbf{H}_0^{ir1}$ on the sample's width and thickness. In order to satisfy Equation (1), charge is required in each half of the sample for the compensation of the external field in the regions where the dipole direction strongly deviates from $\mathbf{H}_0$. The total amount of charge in each half can be derived from the magnetization at the cross section in the middle of the sample by employing Gauss's theorem. The position of the center of the Bloch wall can be used as a measure for the charge stored in each half, which is predominantly located at the object's boundaries. Since a sample having a smaller width needs, at the same $\mathbf{H}_0$, a greater amount of the charge per unit of the width of the cross section in each half to cancel the same $\mathbf{H}_0$, it follows that the wall reaches the edge at a lower field $\mathbf{H}_0^{ir1}$ in the samples of smaller width.

This is confirmed by the experiments (see **Table 2**). Since in all cases the film thickness is very small in comparison to its width and length and $\mathbf{H}_0$ is a uniform field, the surface-charge pattern required is, in a first-order approximation, independent of the thickness of the sample. As a consequence, the $\mathbf{H}_0^{ir1}$ of thicker samples is larger than the field required for thinner samples (see Table 2). It can be seen in Table 2 that $\mathbf{H}_0^{ir1}$ for the 700-Å-thick lift-off layers divided by $\mathbf{H}_0^{ir1}$ for the sputtered layers with equal dimensions is 0.274, 0.290, and 0.390 for the samples with widths of 30, 20, and 10 μm, respectively. The thickness ratio of the lift-off to sputtered samples is 0.28, so there is good quantitative agreement, in particular for the samples with widths of 30 and 20 μm.

Furthermore, note that the curves of the Bloch wall position in Figure 39 belonging to increasing and decreasing fields of the sputtered sample almost coincide, which shows that the wall friction inside the specimens is rather small. This might be anticipated because of the low value of the wall-friction field $\mathbf{H}_f$ in comparison with $\mathbf{H}_0^{ir1}$. In addition, note that most of the change in $\mathbf{M}$ consists of a rotation of about 180° of the dipoles in the region covered by the movement of the Bloch wall. As a consequence, the anisotropy energy of the samples is hardly affected.

As stated, the Bloch wall midpoint touches the edge at field $\mathbf{H}_0^{ir1}$. A further slight increment in $\mathbf{H}_0$ lets this wall be torn apart into two pieces. The subsequent sudden shrinkage in its length causes a large portion of the 180° wall to collapse; no doubt an irreversible transition is involved. Judging from the area of the triangular tip domains just before and after the transition, this irreversible event is accompanied by a rotation of $\mathbf{M}$ in the direction of $\mathbf{H}_0$.

As soon as $\mathbf{H}_0$ has exceeded this critical value, we can be assured that the field penetrates into the sample, because no extra charge is available for compensating $\mathbf{H}_0 - \mathbf{H}_0^{ir1}$. It is often observed that the ferrofluid is asymmetrically distributed with respect to the longitudinal axis of the sample. More ferrofluid is found

at the sides of the triangular domains that contain the edge doublets. Consequently, the field penetrates at these values of $\mathbf{H}_0$ into the opposite side in the middle portion of the sample. This indicates that an asymmetric distribution may already be present when $\mathbf{H}_0 < \mathbf{H}_0^{ir1}$, implying that the field penetration has already taken place in an earlier stage.

A surviving part of the Bloch wall reveals itself near each sample tip [see Figure 38(d)]. Note that this wall does not touch the edge any longer and is at an angle. In the subsections on edge clusters and (sub)cluster creation and fading, we concluded that a second wall, i.e., an edge doublet, must reveal itself. This second wall is very visible near one of the doublet knots in Figure 38(d). It must have developed along a creation line and, subsequently, must have increased its angle, so that it possibly has a Néel structure. This opinion is supported by an estimation of the wall angles based on Equations (12d) and (12e), with $\alpha_1 = 20°$ and $\alpha_2 = 106°$. We estimate that $|\psi| = 40°$ for the new wall and 144° for the Bloch wall. The better visibility of the small-angle wall can only be traced back to a difference in the internal structure. Note that **M** near the doublet knot is still at a small angle [4°; see Equation (12a)] to the edge.

Upon a further increment in $\mathbf{H}_0$, these doublet knots are pushed along the edge toward the sample ends. During this movement the knots sometimes temporarily hold at some points and subsequently catch up by fast displacements. When $\mathbf{H}_0$ reaches the maximum, $\mathbf{H}_0^{max}$, both doublet knots are at the shortest distance from the tip. When $\mathbf{H}_0$ is increased to higher values, a second irreversible jump takes place at which the triangular domain with the doublet knot as a vertex collapses. In this case, the continuous **M** distribution arises with the dipoles pointing toward the object corner [discussed extensively in the subsection on corner clusters; see also Figures 26(a) and 28]. For this experiment, the external field is kept below the critical value at which this second irreversible transformation takes place.

• *Transformations on the descending flank of the B–H loop*

As yet we have reported no significant impact of the influence of the manufacturing technique and the magnetic anisotropy on domain behavior in thin films. These effects are revealed, and are much more pronounced, on the descending flank of the B–H loop. Our discussion is based mainly on the very soft Permalloy (83 Ni 17 Fe) composition, in which the role of defects dominates, while the influence of the anisotropy is mentioned briefly. A remarkable incongruence between the domain-structure development of the sputtered and lift-off samples comes to light. The simpler of the two, the sputtered sample, is discussed first.

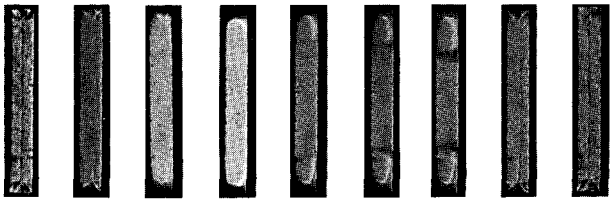


**Figure 40**

Domain conversions in a sputtered sample measuring 60 × 10 μm and 2500 Å thick, as a function of $\mathbf{H}_0$, which increases from 0 in part (a) to 2740 A/m (= 34.4 Oe) in (d) and as $\mathbf{H}_0$ decreases uniformly starting in (e) and reaching 0 in (i).

*Sputtered sample*

**Figure 40** shows a long rectangular specimen (60 × 10 × 0.25 μm) in which the uniform external field parallel to the longitudinal axis increases from zero in Figure 40(a), via $\mathbf{H}_0^{ir1}$ in 40(c), to the maximum $\mathbf{H}_0^{max} = 2740$ A/m in 40(d). Upon a subsequent reduction in $\mathbf{H}_0$, both doublet knots can be seen to have been shoved toward the middle. Note that these knots in Figure 40(g), a photograph taken just before the second irreversible jump at $\mathbf{H}_0^{ir2}$, are much closer to the center of the sample than at $\mathbf{H}_0^{max}$; the knot displacements are mainly reversible, although, as on the ascending flank, some interference of defects can be observed. At $\mathbf{H}_0^{ir2}$, a jumpwise transformation takes place from the configuration of Figure 40(g) toward the one in 40(h). A rough estimation of the object's mean $\langle \mathbf{M} \rangle$ component along $\mathbf{H}_0$ in Figures 40(g) and 40(h) reveals a significant alteration ($\Delta \langle \mathbf{M} \rangle \simeq 0.4 M_s$), so that, just as at $\mathbf{H}_0^{ir1}$, the irreversible jump at $\mathbf{H}_0^{ir2}$ is accompanied by magnetic hysteresis. A further reduction in $\mathbf{H}_0$ causes the 180° wall to return to the specimen's central (long) axis at $\mathbf{H}_0 = 0$ [Figure 40(i)], so that the object's hysteresis curve exhibits the course of **Figure 41**. Note that defects are not essential in this hysteresis effect. Moreover, it should be mentioned that the above evolution is advanced by a longitudinal uniaxial anisotropy, as is elucidated in the next section.

*Lift-off sample*

As in the sputtered sample, both edge doublets in the lift-off sample initially tend to move toward the longitudinal center upon a reduction of the longitudinal field $\mathbf{H}_0$. However, this time the doublet knot is held up during the reduction phase of $\mathbf{H}_0$.

At the ends of the sample, the **M** direction deviates strongly from the direction of $\mathbf{H}_0$, while it is parallel to $\mathbf{H}_0$ in the central portion of the sample. Obviously, the total charge available for each half of the sample is collected in the ends, where it tends to cancel $\mathbf{H}_0$. In the

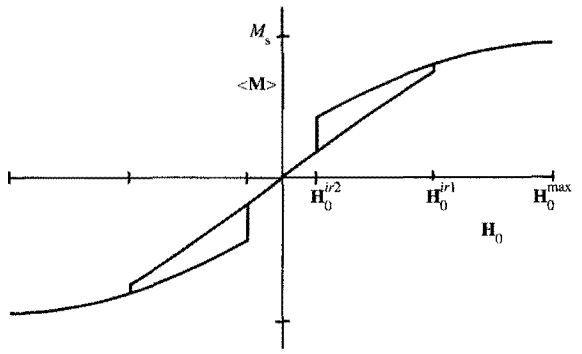


**Figure 41**

A typical hysteresis curve of a sputtered film sample where <**M**> is the object's mean **M** component in the direction of $\mathbf{H}_0$.

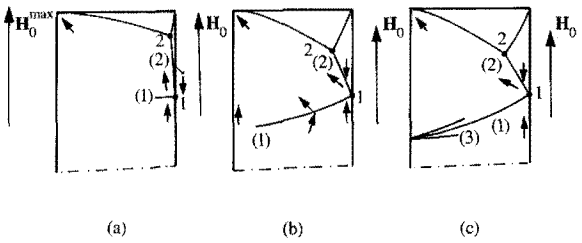


**Figure 42**

(a) Knot 1 just before fixation. (b) Rotation of the doublet walls and the **M** rotation caused by a charge spreading upon further reduction in $\mathbf{H}_0$ after the fixation of knot 1. (c) The edge-triplet creation with a knot at the opposite edge.

hypothetical case in which this charge pattern does not vary after the doublet's stagnation, the resulting micromagnetic $\mathbf{h} = \mathbf{H}_d + \mathbf{H}_a + \mathbf{H}_0$ (in which $\mathbf{H}_a$ is caused by the intrinsic anisotropy) arises in these end domains as $\mathbf{H}_0$ is further reduced. The net field **h** cannot be parallel to **M** here, so that the charge near each end, whose amount is fixed as long as **M** is parallel to $\mathbf{H}_0$ in the midplane perpendicular to the sample longitudinal axis, has to be distributed over a large area near the end.

This enlargement is accomplished by rotating the doublet walls about its knot and by increasing the length of wall (1) in **Figure 42**. The angle enclosed by both doublet walls remains about 90° during the rotation, since **M** remains almost parallel to the edge on both sides of the doublet knot. Therefore, given the fixed doublet knot, the rotation of the doublet walls is closely related to the displacement of free-triplet knot 2 relative to doublet knot 1. This rotation causes **M** between the doublet walls to rotate in the direction perpendicular to the longitudinal sample axis. This tendency is enhanced when the easy uniaxial anisotropy axis is normal to the sample length; the doublet knot is inclined to proceed along the edge when the anisotropy axis is in the direction of the sample length.

In the case that the doublet knot keeps its position, the decreasing external field causes domain wall (1) to increase in length in order to spread the tip charge over a large area. As a consequence, the extremity of wall (1) threatens to coincide with the opposite sample edge.

As discussed in the subsection on (sub)cluster creation and fading, an edge cluster comes into being with a knot at the left edge and at the extremity of the orthogonal trajectory that extends domain wall (1) in the originally continuous **M** region between the tip of wall (1) and the left edge. Wall (1) serves as the seed wall of the edge triplet. Of course, this cluster will be an odd edge cluster, since the **M** directions in the outermost domains are parallel. Usually, the simplest configuration possible—the edge triplet—will develop. Observe the rotation sense of the **M** jump across wall (1) near knot (1). It is obvious that only the chirality of the middlemost wall of the newly formed edge cluster fits that of seed wall (1). Initially, all triplet domain walls coincide with the creation line, while all three wall angles are then zero. A subsequent decline in $\mathbf{H}_0$ causes the triplet to unfold by both outermost walls rotating around their knot [see Figure 42(c)] in the opposite direction with respect to the middlemost one, i.e., seed wall (1). Simultaneously, the wall angles of all three walls must grow from zero to some finite value.

These walls are all of the symmetric Néel type because of the growth of the wall angles of all three walls from zero [70]. This wall structure is preserved during their further development. To balance the exchange torques in the cores of these walls, a charge distribution with dipole character—called the wall dipole—is induced in each core, in which the dipole vector is perpendicular to the wall surface. The ultimate direction of this wall dipole is parallel to the **M** direction in the middle of the Néel wall, as we shall see. As stated above, the field of the wall dipole balances the exchange torques $\mathbf{L}_{ex}$ in the wall core; the directions of $\mathbf{L}_{ex}$ depend on the chirality of the wall [see **Figure 43(a)**]. In general, these exchange torques tend to rotate the dipoles in the core parallel to the dipole direction in the middle of the core. In Figure 43, in which the triplet walls are schematically depicted as being

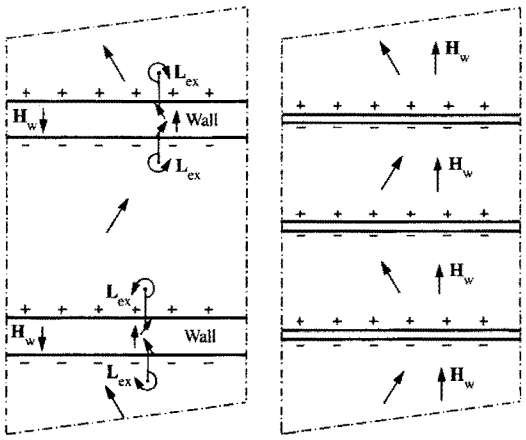


Figure 43

(a, b) The torque equilibrium in the domain-wall cores of a triplet. $\mathbf{H}_w$ is the wall-dipole field and $\mathbf{L}_{ex}$ is the exchange torque.

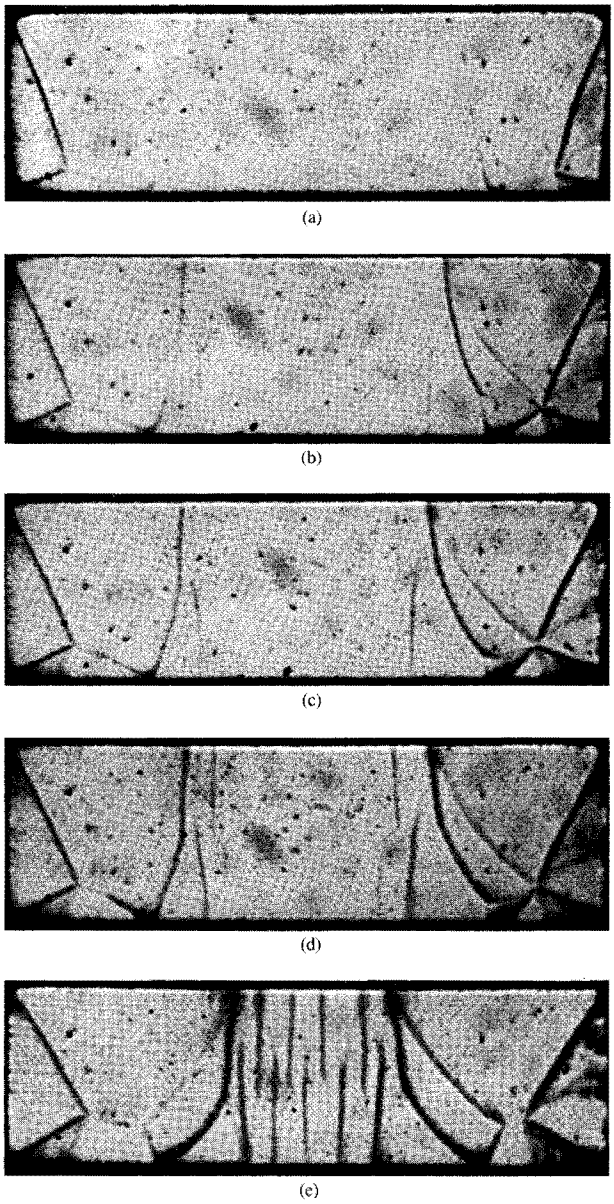


Figure 44

The development of the concertina structure (CS) as $\mathbf{H}_0$ decreases from (a) to (e). Permalloy (60 × 20 μm, thickness 2500 Å).

parallel, these exchange torques are indicated. Note that the wall-dipole field $\mathbf{H}_w$, which balances $\mathbf{L}_{ex}$, always has a component opposite to the core magnetization, and that all wall dipoles point approximately in the direction of $\mathbf{M}$ at the creation just prior to the creation of the triplet, and are thus about parallel to the external $\mathbf{H}_0$ at that instant. The fringing fields of the wall dipoles inside the domains $\mathbf{H}_w$ are parallel to one another and to $\mathbf{H}_0^{max}$ [see **Figure 43(b)**]. In other words, $\mathbf{H}_w$ forces the magnetic dipoles in the domains to rotate in the direction of $\mathbf{H}_0^{max}$, and this is the origin of the wall hysteresis. A quantitative estimation of its impact is given later in this section.

As an intermezzo, focus again on the anisotropy. It is obvious that a strong longitudinal easy-anisotropy axis tends to prevent the unfolding of the triplet in order to avoid large domains on both sides of the middlemost wall of the triplet, where $\mathbf{M}$ deviates strongly from the easy direction. The opposite occurs when a strong easy axis is perpendicular to the longitudinal axis of the specimen. Triplet wall (3) [see Figure 42(c)] rotates strongly and increases simultaneously in length in order to optimize the region where $\mathbf{M}$ turns toward the easy axis; however, this is all subjected to the requirement of the stability of $\mathbf{M}$, in which the magnetostatic torques still play the dominant role.

A further reduction in $\mathbf{H}_0$ causes wall (3) to approach the opposite specimen edge, so that the game of edge-triplet creation has to be repeated. This time, wall (3) in Figure 42(c) constitutes the innermost wall of the new edge triplet with a knot at the right edge. This coherence can be comprehended by comparing the chiralities of the newly created edge-triplet walls with one of the seed wall (3). Again, the wall dipoles of these newly added walls are parallel to $\mathbf{H}_0^{max}$ and thus increase the magnetic hysteresis. This triplet creation process repeats itself upon further reduction in $\mathbf{H}_0$ (see **Figure 44**). These triplets can be

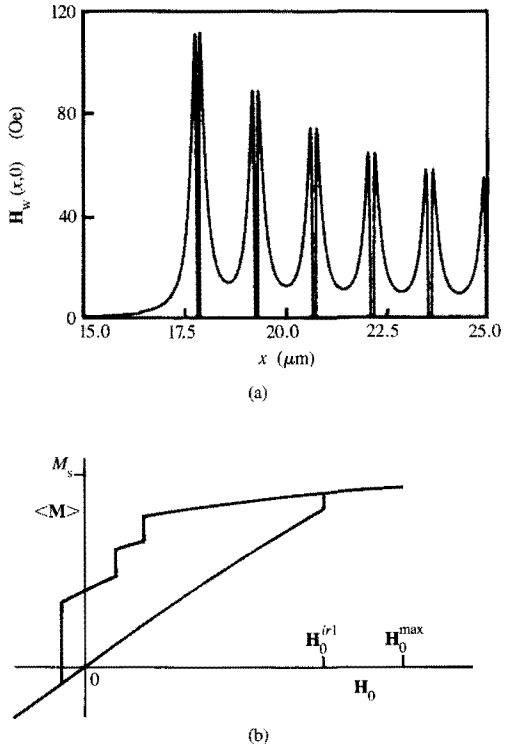


**Figure 45**

(a) The wall-stray field $\mathbf{H}_w$ inside the domains. (b) The hysteresis curve of an element that contains a CS.

removed again in a continuous fashion by an intermediate period of increasing $\mathbf{H}_0$, which indicates that the edge-cluster additions are reversible, notwithstanding their contribution to the hysteresis.

It often occurs that the doublet knot performs a jumpwise displacement to a subsequent stagnation point. This unstable character of the doublet-knot position shows that pinning must be involved. Along with the doublet-knot displacement, a fraction or all of the already created edge triplets disappear, so that the wall hysteresis is reduced. It should be emphasized that the edge-triplet knots jump less frequently, while, in addition, such a jump has less impact on the rest of the domain structure. This distinction can be understood because **M** near and in the doublet knot deviates strongly from the continuous nearly uniform **M** distribution in the domains, while, contrary to this, an edge-triplet knot resembles very closely a uniform **M** state, in particular when the unfolding of the edge triplets is impeded by a strong longitudinal easy-anisotropy axis. Therefore, the edge-doublet knots get pinned more easily and strongly. Judging from the difference in behavior between the sputtered and the lift-off samples, it is likely that the latter possess stronger pinning points at their edges.

Ultimately, the middle portion of the sample is filled with edge triplets that constitute a bellows-like configuration, the so-called concertina structure (CS). At a given $\mathbf{H}_0$, the number of walls in and the space occupied by the bellows generally increase proportionally with increasing $\mathbf{H}_0^{max}$; as a consequence, the wall hysteresis is a semipositive definite function of $\mathbf{H}_0^{max}$. To estimate the wall hysteresis, it is necessary to know the dipole distribution in the wall core which in thin layers can be derived from the one-dimensional micromagnetic calculations of Riedel et al. [71]. **Figure 45(a)** gives a quantitative image of the mean $\langle \mathbf{H}_w \rangle$ across the sample thickness for the domain structure of Figure 44(e), where $x$ is along the sample length and $x = 25$ $\mu$m in the middle of the sample. $\langle \mathbf{H}_w \rangle$, which exhibits strong peaks much larger than $\mathbf{H}_k$ near the wall cores, must be almost completely canceled by the stray-field $\mathbf{H}_s$ in this soft-magnetic element. For this compensation, there must be a net magnetic charge in each sample half, which is supplied through a net **M** component normal to the sample's midplane that is perpendicular to the sample length. The wall hysteresis **[Figure 45(b)]** for this particular situation was previously estimated [49, 51] and the mean **M** component of the object along the $x$-direction amounted theoretically to $0.25M_s$, while the experimental hysteresis was almost twice as large. This difference may be due to other hysteretic effects and/or to the simplifications in the theoretical model. However, the significance of wall hysteresis in these thin elements is beyond dispute. A similar result for simpler but similar domain configurations was reported by N. Smith [72].

*Demolishment of the concertina structure*

It is obvious that the concertina structure (CS) constitutes a metastable high-energy state and that energy may be gained by removing periods of the bellows-like structure.

**Figure 46** provides an example of a very simple CS, in which the central walls of three adjacent edge triplets in the sample are replaced by the central wall of one edge triplet. Note that the wall angles of the three central walls in Figure 46(a) deviate significantly from 180° (≃160° according to the cluster relation), so that the mean magnetization along the longitudinal sample axis in the middle of the sample is still of significance.

The period reduction can be briefly summarized as follows. An edge quintet is formed after the fusions of the two triplet knots at the bottom edge. This conversion is followed by a furcation of the quintet into an edge-triplet knot and a free-triplet knot. The latter moves upward along the central wall of the quintet and thus removes the

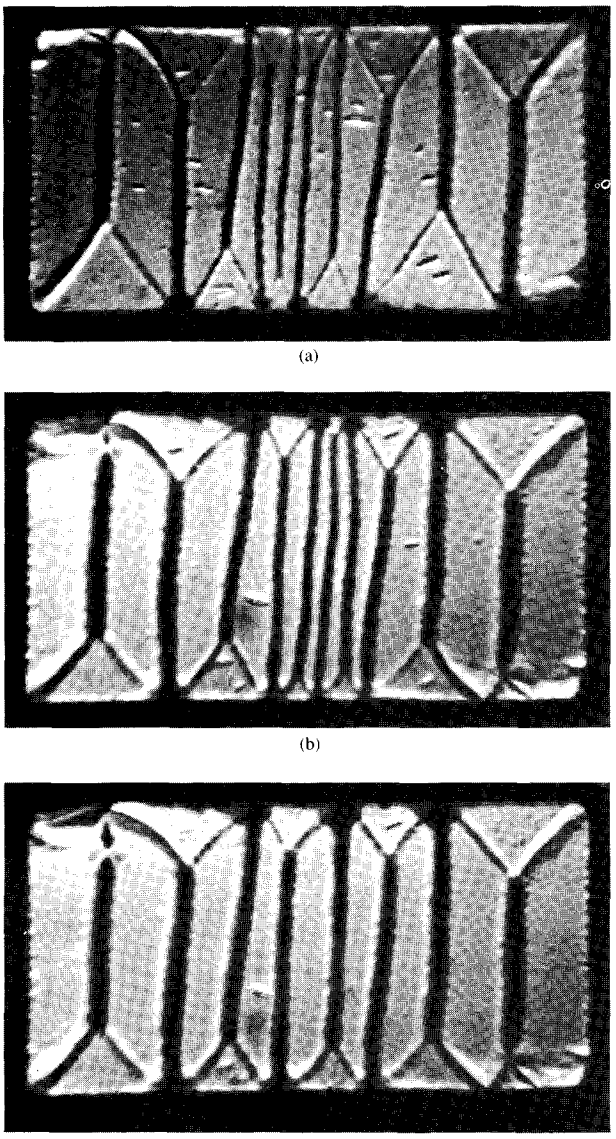

Figure 46

Period reduction in a CS. The central walls of three adjacent edge triplets in (a) are replaced by one central wall in (c). All images are at approximately the same $\mathbf{H}_0$. Permalloy (60 × 30 $\mu$m, 700 Å).

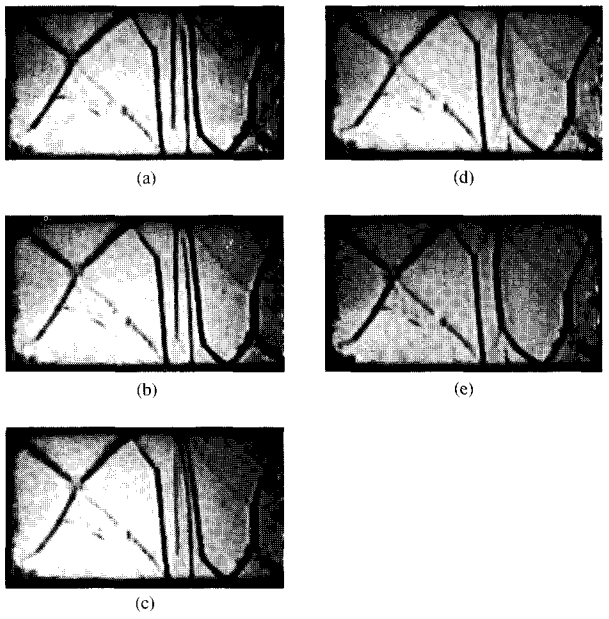

Figure 47

The sequential frames of a video display of a period reduction in a simple CS. Permalloy (60 × 30 $\mu$m, 700 Å).

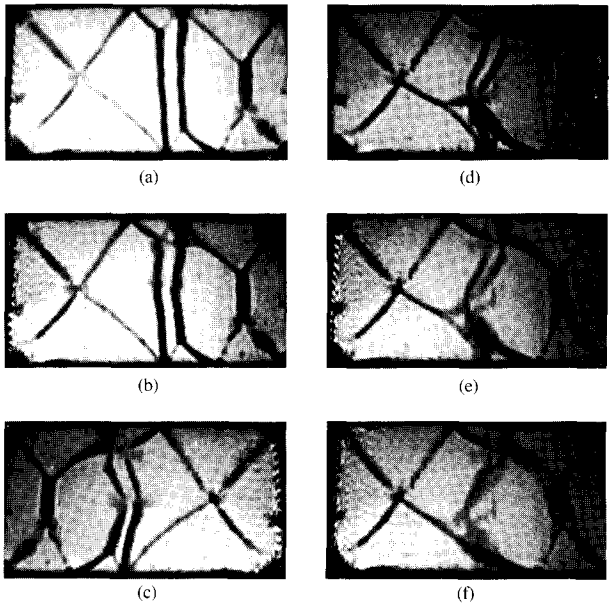

Figure 48

The period reduction by a coherent movement of a uniform quartet and a free cluster at the adjacent central walls of two edge triplets. Permalloy (60 × 30 $\mu$m, 700 Å).

two outermost central walls of the original three edge clusters. The details of this fusion and subsequent furcation can be better discerned in **Figure 47**, which shows the sequential frames of a video display.

After the reduction, the mean $\mathbf{H}_w$ of the sample has reduced and a charge redistribution takes place. This charge displacement can also be deduced from the wall angle of the remaining central triplet wall in Figure 46, which increases to about 180°. A similar increase in the

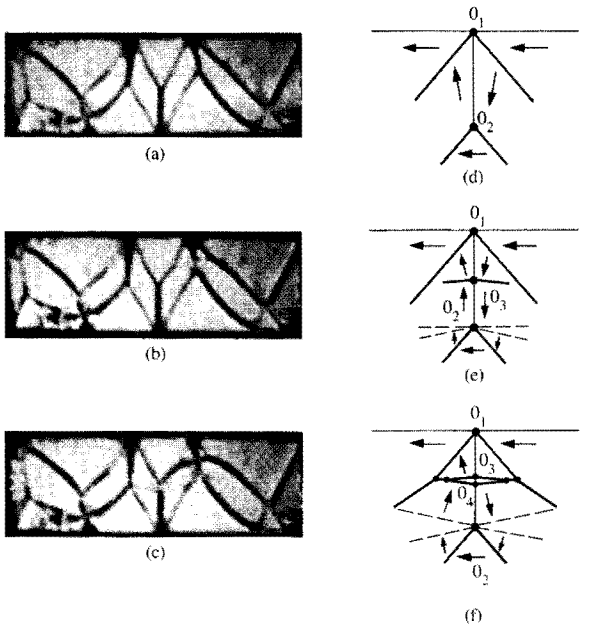


**Figure 49**

The inversion of the polarity of the Néel walls in a 140-$\mu$m-thick Permalloy layer (60 × 20 $\mu$m).

wall angle can also be noted in Figure 47. Both observations confirm our previous conclusion that the impact of the wall-hysteresis mechanism is significant.

The details of the same type of period reduction are strongly dependent on film thickness. In very thin layers (25 nm), the Néel walls are very persistent and the CS is also sustained when $\mathbf{H}_0$ is inverted. Domain walls with angles up to 360° are developed before they are demolished. In 70-nm-thick layers, the period reductions are often attended by the propagation of free uniform quartets (crosses) and free doublets with two rotation segments (Bloch lines), demarcating Néel-wall segments with opposite chiralities. Thus the wall field $\langle \mathbf{H}_w \rangle$ of the original Néel walls is reduced. **Figure 48** demonstrates this principle in a very simple CS. In the middle of the sample, two central walls of edge triplets with an angle of about 160° reveal themselves. This time, the conversions cannot be heralded by the fusion of two edge-triplet knots. Instead, a uniform free quartet arises at the tip of the left central edge-triplet wall, while, simultaneously, a uniform free quartet and free doublet develop at the right central wall. The latter doublet, together with the free quartet at the left wall, moves downward, while the polarity of the Néel wall segments above this pair is inverted. In a second phase, the moving quartet knot and doublet knot, at which the latter presumably has been converted into a free-triplet knot by incorporating one of the walls of the quartet, come together and fuse. Subsequently, the Néel wall segments at both sides of this fused-knot pair shrink and disappear.

A final example of a transformation in a 140-$\mu$m-thick Permalloy layer is shown in **Figure 49**. Again, the conversions start at the domain walls with the largest wall angle, i.e., the central triplet wall at the right ($|\psi| \simeq 150°$). Again, a uniform quartet develops itself at the free triplet bounding the central wall in question [Figure 49(a)]. Simultaneously, a furcation takes place and the quartet moves upward. This time, the quartet does not separate into two Néel wall segments with opposite polarity; instead, it transforms the original Néel wall into a Bloch wall [Figure 49(b)]. Upon a further reduction in $\mathbf{H}_0$, a new uniform quartet develops itself at the same free triplet and moves upward. The sector angle of the rotation segments of the free triplet in question increases and causes the outermost wall of the edge triplet to become curved parabolically [Figure 49(c)]. Both knots of the above quartets and the knots of two extra free-triplet knots, which arise at the intersection of the "wings" of both quartets, fuse and a uniform quartet results. Thus, the polarity of the Néel wall has been inverted between the knots of the free triplet and the uniform [Figures 49(d–f)] quartet. Note that the same process takes place almost simultaneously at the other central walls of the edge triplets, so that nearly the entire domain structure is converted in one coherent transformation.

It is self-evident that the above period reductions and coherent conversions cause the stepwise course of the object's $\mathbf{M} - \mathbf{H}_0$ hysteresis loop, as is schematically presented by Figure 45(b). The CS endures much longer in the case of a strong easy axis perpendicular to the sample length. In this case, the reversal of the polarity of the wall dipoles is accomplished by free-quartet and free-doublet generations and displacements, so that the CS can survive when $\mathbf{H}_0$ is reversed.

• *Discussion*

The central themes of Section 4 are the conditions and the modes for reversible and irreversible changes in the domain structure in soft-magnetic thin-film elements. We have confined ourselves to the rectangular sample; however, it should be emphasized that the above order presents itself in thin-film elements with arbitrary geometry. Whether or not a CS develops depends on the orientation and strength of the uniaxial anisotropy and on the presence and nature of defects. In particular, the lift-off sample tends to possess edge defects to which doublet knots, in particular, adhere, thus giving rise to CS development in very soft media. On the other hand, the CS creation is also facilitated when the relatively strong

easy axis is perpendicular to both $\mathbf{H}_0$ and the object length, while an only slightly hindered movement of both doublets toward the middle takes place when the easy axis is parallel to $\mathbf{H}_0$.

Much emphasis has been put on the orientation of the walls with respect to $\mathbf{H}_0$, their internal structures, their stray fields $\mathbf{H}_w$, and on the resulting wall hysteresis of the CS. Note that, in principle, there is no correlation between the energy stored in the domain walls and their contribution to hysteresis. This is convincingly demonstrated by the single and double Landau–Lifshitz structures illustrated in **Figure 50**, where the 180° walls are assumed to be of the Bloch type which induce no net $\mathbf{H}_w$ [70]. It is obvious from the symmetry of the dipole charge distributions in the various wall cores in Figure 50(a) that the net effect is zero, so that the wall hysteresis is zero. The same argument applies to the double Landau–Lifshitz structures of Figure 50(b); we have two configurations with different wall energies and the same zero hysteresis.

The CS is reminiscent of the ripple structure in thin films, which encourages us to draw a parallel. It is well known that the ripple structure originates in the dispersion of the anisotropy, which causes **M** to split up into a great number of domains separated by parallel walls normal to the mean **M**. This wall splitting becomes particularly manifest when $\mathbf{H}_0$ is perpendicular to the easy axis [73–76].

In the previous section, we stated that the development of the CS in thin-film objects with small lateral dimensions originates in the spreading of the magnetic charge in the sample tips upon decreasing $\mathbf{H}_0$, which requires discontinuities in **M**, e.g., wall surfaces, between the longitudinal edges. As in the solenoidal situation, the domain-wall pattern is predominantly governed by magnetostatic laws; however, these allow a great variety of solutions at each $\mathbf{H}_0$ value. The ultimate selection from the possible domain-structure developments is controlled by a large number of second-order parameters such as defects and the magnitude, symmetry, and direction of the anisotropy and also, no doubt, by stochastic variations in the latter parameters. Though the stochastic variations may play a role, they are not a prerequisite for CS development, as evidenced by the occurrence of CSs in perfect crystallites [36].

We can make the argument concerning the dominance of magnetostatics a little more explicit. During the discussion of Figure 42, we emphasized that doublet wall (1) must grow in order to distribute the positive charge in that sample end over a larger area during the reduction phase of $\mathbf{H}_0$. Note that **M** values near the opposite edges at the height of the doublet knot are about parallel and are inclined to bend outward a little bit in the particular end. Charge of the wrong sign threatens to arise. In order

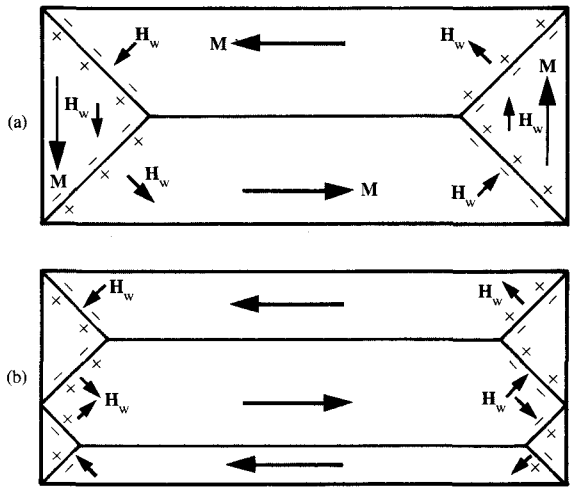


**Figure 50**

(a) Landau–Lifshitz structure in a rectangular sample in which the only 90° walls are Néel walls. (The field $\mathbf{H}_w$ and magnetic charges of these walls are indicated.) (b) The double Landau–Lifshitz structure.

to get the desired positive charge density, a domain wall must be present between the above edges, so that an additional jumpwise **M** direction change, which is accompanied by a net charge generation, is introduced.

Consider another striking manifestation of magnetostatics; in the CS, the edge-cluster walls constitute a periodic pattern of clearly visible walls normal to the longitudinal sample edge, where both patterns with knots on the opposite edge have a phase shift of 180°. This order is certainly not characteristic of ripple. Note that **M** rotates over a finite angle between two adjacent clearly visible walls at the same longitudinal sample edge. As a consequence, one extra wall must arise from each of these edge-cluster knots between the corresponding clearly visible walls. We have already concluded that both edge clusters have to be triplets, although their exterior walls are often hardly visible. Thus, along a specific edge, we see alternately an **M**-direction jump at a clearly visible wall and about the same rotation in **M** divided over the walls. This order cannot be explained in terms of ripple theory and reflects the magnetostatic coupling of two adjacent clearly visible walls.

We return to the sample with a longitudinal weak easy axis, in which $\mathbf{H}_c$ is smaller than $\mathbf{H}_k$. The CS is frequently

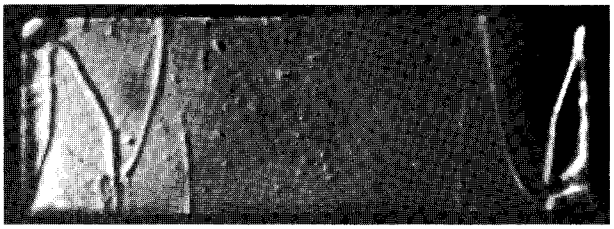

(a)

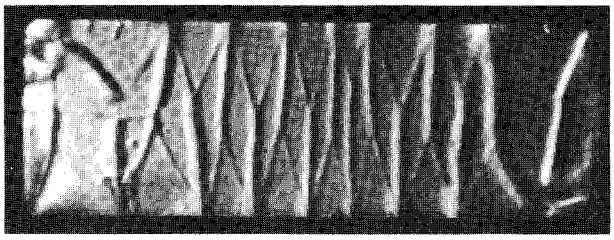

(b)

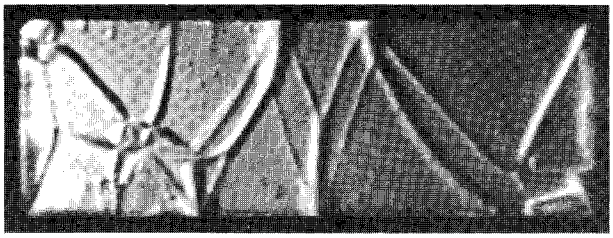

(c)

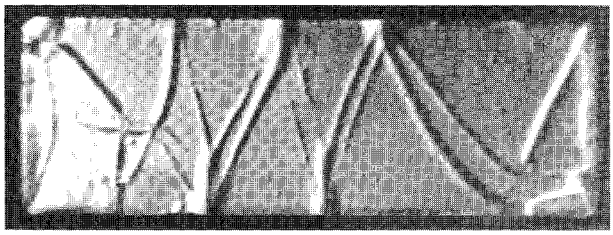

(d)

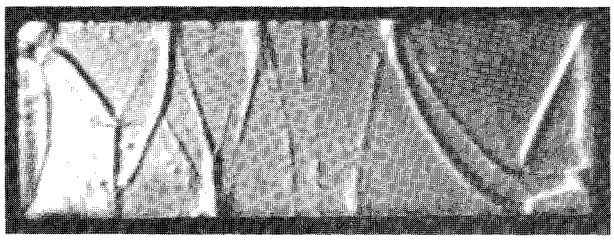

(e)

**Figure 51**

The recovery of the CS periods by increasing $\mathbf{H}_0$ toward $\mathbf{H}_0^{max}$. (b, c) Transformations when $\mathbf{H}_0$ is decreased from $\mathbf{H}_0^{max}$ in (a). (d, e) Recovery of the periods upon an increment in $\mathbf{H}_0$ in its original direction. $\mathbf{H}_0$ is parallel to the long axis of the specimen in each case.

observed in such samples, notwithstanding the noninverted character of the medium [73]. When discussing the lift-off sample, we emphasized the impact of the doublet pinning at edge defects. One might state that this pinning prevents the sample from "switching" its magnetization pattern by the wall (doublet-knot) displacement, and that the edge defects play the role of the "object invertor." A prolonged reduction in $\mathbf{H}_0$ causes the effective micromagnetic field in the region in front of doublet wall (1) (see Figure 42) to become zero, so that the discontinuity in **M** at wall (1) is allowed to extend into the interior of the sample; e.g., wall (1) elongates. This growth in which the newly formed walls are initiated by and connected to the walls already present in the CS has often been observed. In this process, stochastic anisotropy variations affect the path along which wall (1) grows; however, these possible trajectories are confined to a small band defined by the local spatial steepness of the demagnetizing field due to the charge pattern in the sample tip, while directional variations of the walls which are too abrupt are staved off by the well-known transverse magnetostatic coupling [73, 75]. Bear in mind that, in general, the **M** environment which suppresses the inclination of the dipole to follow the local anisotropy direction is not uniform, and that it is embedded in the overall **M** distribution of the sample, to which it is magnetostatically coupled. Again, the dominance of magnetostatics is evident.

One final observation concerns the dissolution of a number of the periods of the CS when the edge-doublet knot performs a jumpwise movement. In ripple terminology, one might say that the sample inversion is abolished, so that switching takes place by wall movement, and, of course, ripple no longer appears. However, the above consequence of doublet displacements applies to samples with both a longitudinal and a transverse weak easy axis, so the above explanation is too innocent. In this context, the progress of the configuration in **Figure 51** is of interest. From the saturated state, the domain structure develops via the configuration of Figure 51(a) into the CS of Figure 51(b). Upon a further reduction in $\mathbf{H}_0$, period reductions take place, so that we end up with Figure 51(c). Subsequently, the field is increased again, and the domains with **M** direction deviating from $\mathbf{H}_0$ shrink. Note that the magnetization in the small domains in the middle of the sample is at an angle of about 30° to $\mathbf{H}_0$. A small further increment in $\mathbf{H}_0$ causes the reappearance of two of the periods of CS, when the original edge-triplet knots in the middle of the sample move apart. Apparently, the recovery of these periods is required in order to obtain a stable **M** distribution in the middle of the sample that matches the given **M** configurations in both tips. Again, these periods of the CS seem to have a deterministic origin rather than a stochastic one, and the ripple theory leaves us in the lurch.

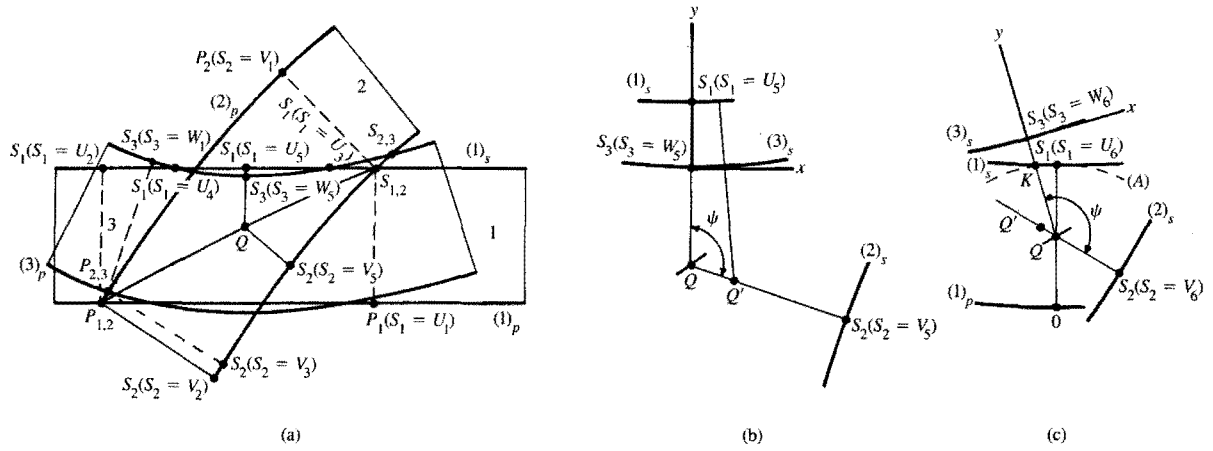


**Figure 52**

(a) Three successive parallel segments (1)–(3), and the wall-shape determining edge segments. (b) Construction when edge $(3)_s$ is on the wrong side of edge $(1)_s$. (c) Construction when edge $(3)_s$ is on the right side of edge $(1)_s$.

## Appendix A

Let us consider three successive parallel segments (1) to (3) and investigate whether there are restrictions on their shapes and mutual positions. In the subsection on parallel subregions, the only requirement from the mutual positions of two adjacent segments (1) and (2) is the existence of two intersection points $S_{1,2}$ and $P_{1,2}$. The course of the separating domain wall between (1) and (2) is governed by the edge segments $S_{1,2}S_1(s_1 = u_2)$ and $S_{1,2}S_1(s_1 = v_2)$ at edges $(1)_s$ and $(2)_s$, respectively, or equivalently, by edge segments $P_{1,2}P_1(s_1 = u_1)$ and $P_{1,2}P_2(s_2 = v_1)$ [see **Figure 52(a)**]. Even so, the domain wall between the parallel segments (2) and (3) is governed by the edge segments $S_{2,3}S_2(s_2 = v_3)$ and $S_{2,3}S_3(s_3 = w_1)$. The position of $P_{2,3}$ at edge $(2)_p$ with respect to $P_{1,2}$ must comply with the course of **M** along the edge and the numbering of the segments. The same applies to the position of $S_{2,3}$. The fulfillment of these requirements is considered to be a prerequisite.

However, in addition we require that the domain wall between $P_{2,3}$ and $S_{2,3}$ not intersect the one between $P_{1,2}$ and $S_{1,2}$. We shall prove that this requirement is satisfied when the domain wall codetermining part of edge $(3)_s$, $S_{2,3}S_3(s_3 = w_1)$, does not intersect the domain wall codetermining part of edge $(1)_s$, $S_{1,2}S_1(s_1 = u_2)$.

We first investigate the situation in which $(1)_s$ and $(3)_s$ intersect at the points $S_1(s_1 = u_4)$ and $S_1(s_1 = u_3)$. By virtue of the continuity of the tangents to the edges of the segments, it can be concluded that there exists a point at $(1)_s$, say $S_1(s_1 = u_5)$, where the characteristic base curves of the parallel segments (1) and (3) coincide. This base line intersects the domain wall between segments (1) and (2) at $Q$, where the distance $|S_1(s_1 = u_5)Q| = |S_2(s_2 = v_5)Q|$. It is obvious that $|S_3(s_3 = w_5)Q| < |S_1(s_1 = u_5)Q|$. Now look for the position of the points of the domain wall between segments (2) and (3) at the base line through $S_2(s_2 = v_5)$, and call the points of intersection of the latter base line with the characteristics of (3) $Q'$. We erect a Cartesian coordinate system with its origin at $S_3(s_3 = w_5)$ and a $y$-axis along the base curve through $S_1(s_1 = u_5)$ [see **Figure 52(b)**], while the positive $x$-axis is on the side where the angle $\psi$ between the characteristics at $Q$ is smaller than $\pi$. At a sufficiently small $x$, the edge $(3)_s$ can be approximated by the quadratic relation $y = ax^2$ with $|a| < 1/(2b)$, where $b$ is the segment width. In a first-order approximation, the difference in distance of $Q'$ from edges $(1)_s$ and $(3)_s$ as a function of $x$ decreases by

$$(1 - \cos\psi)/\sin\psi(1 + 2a|S_3(s_3 = w_5)Q|).$$

Observe that $(1 - \cos\psi)/\sin\psi$ is larger than zero because $0 \le \psi \le \pi$ and that $(1 + 2a|S_3(s_3 = w_5)Q|) > 0$, since $|2a| < 1/b$ and $|S_3(s_3 = w_5)Q| < b$. As a result, the absolute value of the mutual difference in the distance of $Q'$ from edges $(1)_s$ and $(3)_s$ decreases for positive $x$. It is obvious that $Q'$ moves toward edge $(2_s)$. This tendency is also preserved at large $x$, because the base lines of parallel segment (3) do not intersect each other inside (3). Therefore, the ultimate $Q'$ at the domain wall between segments (2) and (3) is on the wrong side of the domain wall between segments (1) and (2).

Now we attempt to prove that all points of the wall between segments (2) and (3) are correctly situated with respect to the wall between points $S_{1,2}$ and $P_{1,2}$ when the edge segments $S_{2,3}S_3(s_3 = w_1)$ and $S_{1,2}S_1(s_1 = u_2)$ do not intersect.

In **Figure 52(c)**, the domain-wall point $Q$ at the characteristic base lines through $S_1(s_1 = u_6)$ and $S_2(s_2 = v_6)$ is indicated. The circle (A) with radius $b$, where $b$ is the segment width, touches at segment edge $(1)_s$ at $S_1(s_1 = u_6)$. Observed from $Q$, the base curve corresponding to $S_3(s_3 = w_6)$ will consecutively intersect circle A, edge $(1)_s$, and finally $(3)_s$. Bearing in mind that the distance $|S_1(s_1 = u_6)Q| < b$, it follows from simple geometrical considerations that $|QK| \geq |S_1(s_1 = u_6)Q|$, so that $|S_3(s_3 = w_6)Q| > |QK| \geq |S_2(s_2 = v_6)Q|$ [see Figure 52(c)].

Having established this fact, we erect a Cartesian coordinate system with its center at $S_3(s_3 = w_6)$, with the $y$-axis along the base line through $S_3(s_3 = w_6)$ and with its positive $x$-axis pointing toward the side where the angle $\psi$ between the characteristics through $S_3(s_3 = w_6)$ and $S_2(s_2 = v_6)$ is smaller than $\pi$. From now on, we can repeat the arguments employed in the previous case. It can be seen for very small $x$ that the distance $|Q'S_2(s_2 = v_6)|$ becomes closer to the distance between $Q'$ and edge $(3)_s$ when moving toward the negative $x$ direction. As a consequence, $Q'$ moves apart from $S_2(s_2 = v_6)$ when $x$ becomes more negative. This tendency is continued at large negative $x$ values because the characteristic base lines of segment (3) do not intersect inside this segment. Thus, if present, the point of the domain wall between the segments (2) and (3) on the base curve through $S_3(s_2 = v_6)$ is found and is at the correct side of the wall in $P_{1,2}$ and $S_{1,2}$.

*Remark*

When edge segment $S_{2,3}(s_3 = w_1)$ does not intersect edge segment $S_{1,2}S_1(s_1 = u_2)$, their counterparts at edges $(3)_p$ and $(1)_p$, respectively, will likewise not intersect.

*Remark*

We have assumed that $P_{1,2}$ and $P_{2,3}$ are different points. It is obvious that the same conclusions apply when $P_{1,2}$ and $P_{2,3}$ coincide.

## References


1. D. A. Herman, B. E. Argyle, and B. Petek, "Bloch Lines, Cross Ties and Taffy in Permalloy," *J. Appl. Phys.* **61,** 4200–4205 (1987).
2. B. E. Argyle, B. Petek, F. Suits, and D. A. Herman, "Bloch Line Influence on Domain-Wall Dynamics in Thin-Film Heads," *J. Appl. Phys.* **63,** 4033–4035 (1988).
3. T. Tsang and S. K. Dekker, "The Origin of Barkhausen Noise in Small Permalloy Magnetoresistive Sensors," *J. Appl. Phys.* **52,** 2465–2467 (1981).
4. T. Tsang and S. K. Dekker, "Study of Domain Formation in Small Permalloy Magnetoresistive Elements," *J. Appl. Phys.* **53,** 2602–2604 (1982).
5. C. S. Comstock, H. Y. Yoo, and A. V. Pohm, "Perturbations to the Stoner–Wolhfarth Threshold in 2 × 2 $\mu$m M-R Memory Elements," *J. Appl. Phys.* **63,** 4321–4323 (1988).
6. G. W. Garnett, W. D. Corner, and D. R. Brambley, "Magnetic Domain Studies in Asymmetric Chevron Bubble Propagation Tracks," *J. Magn. Magn. Mater.* **18,** 1545–1547 (1980).
7. J. C. Slonczewski, B. Petek, and B. E. Argyle, "Micromagnetics of Laminated Permalloy Films," *IEEE Trans. Magnetics* **24,** 2045–2053 (1988).
8. K. Yamada, M. Ohmukai, T. Maruyama, T. Tatsumi, and H. Urai, "CoZrMo Amorphous Films as a Soft Adjacent Layer for Biasing Magnetoresistive Elements with a Current Shunt Layer," *J. Appl. Phys.* **63,** 4023–4025 (1988).
9. N. Smith, "Micromagnetic Analysis of a Coupled Thin-Film Self-Biased Magnetoresistive Sensor," *IEEE Trans. Magnetics* **23,** 259–273 (1987).
10. K. Ounadjela and G. Suran, "Exchange Coupling Between a Soft and a Hard Ferromagnetic Thin Film," *J. Appl. Phys.* **63,** 3244–3246 (1988).
11. J. C. Scott, "Ferromagnetic Resonance Studies in the Bi-Layer System $Ni_{0.80}Fe_{0.20}/Mn_{0.50}Fe_{0.50}$," *J. Appl. Phys.* **57,** 3681–3683 (1985).
12. C. Tsang, P. Kasiraj, and M. Krounbi, "Magnetic Study of Nonlaminated, Bilaminated and Multilaminated Permalloy Stripes," *J. Appl. Phys.* **63,** 2938–2940 (1988).
13. D. A. Herman, B. E. Argyle, B. Petek, L. T. Romankiw, P. C. Andricacos, S. Krongelb, D. L. Rath, D. F. Canaperi, and M. L. Komsa, "Study of Field-Driven Wall Conversions for Laminated Permalloy in the Easy-Axis State," *J. Appl. Phys.* **63,** 4036–4038 (1988).
14. W. F. Brown, *Ferromagnetism*, North-Holland Publishing Co., Amsterdam, 1962.
15. L. Landau and E. Lifshitz, "On the Theory of the Dispersion of Magnetic Permeability in Ferromagnetic Bodies," *Phys. Z. Sowjetunion* **8,** 153–169 (1935).
16. C. Kittel, "Theory of the Structure of Ferromagnetic Domains in Films and Small Particles," *Phys. Rev.* **70,** 965–971 (1946).
17. J. Kaczér and R. Gemperle, "The Thickness Dependence of the Domain Structure of Magnetoplumbite," *Czech. J. Phys. B* **10,** 505–510 (1960).
18. J. Kaczér and R. Gemperle, "A Contribution to the Domain Structure of Iron Whiskers," *Czech. J. Phys.* **9,** 306–313 (1959).
19. Z. Málek and V. Kambersky, "On the Theory of the Domain Structure of Thin Films of Magnetically Uniaxial Materials," *Czech. J. Phys.* **8,** 417–422 (1958).
20. W. F. Brown, *Micromagnetics*, Krieger Publishing Co., Huntington, NY, 1978.
21. A. Hubert, "Stray-Field-Free Magnetization Configurations," *Phys. Status Solidi* **32,** 519–534 (1969).
22. A. Hubert, "Stray-Field-Free and Related Domain Wall Configurations in Thin Magnetic Films (II)," *Phys. Status Solidi* **38,** 699–713 (1970).
23. A. E. LaBonte, "Two-Dimensional Bloch-Type Domain Walls in Ferromagnetic Films," *J. Appl. Phys.* **40,** 2450–2458 (1969).
24. H. A. M. van den Berg, "A Micromagnetic Approach to the Constitutive Equation of Soft-Ferromagnetic Media," *J. Magn. Magn. Mater.* **44,** 207–215 (1984).
25. H. A. M. van den Berg, "Micromagnetics and Domains in Soft-Ferromagnetic Media," Ph.D. Thesis, Delft University of Technology, Netherlands, 1984.
26. I. Sneddon, *Elements of Partial Differential Equations*, McGraw-Hill Book Co., Inc., New York, 1957.
27. H. A. M. van den Berg, "Self-Consistent Domain Theory in Soft-Ferromagnetic Media. I. Solenoidal Distributions in Elliptical Thin-Film Elements," *J. Appl. Phys.* **57,** 2168–2173 (1985).
28. H. A. M. van den Berg, "Self-Consistent Domain Theory in Soft-Ferromagnetic Media. II. Basic Domain Structures in Thin-Film Objects," *J. Appl. Phys.* **60,** 1104–1113 (1986).

29. H. A. M. van den Berg, "A Self-Consistent Domain Theory in Ideal Soft-Magnetic Media," *IEEE Trans. Magnetics* **20,** 1822–1824 (1984).
30. G. W. Garnett, W. D. Corner, and D. R. Brambley, "Magnetic Domain Studies in Asymmetric Chevron Bubble Propagation Tracks and Chevron Detectors," *J. Magn. Magn. Mater.* **15–18,** 1545–1547 (1980).
31. I. Khaiyer, "A Study of Domain Wall and Magnetic Domain Changes in T. Bar by Employing Ferro-Fluid and Comparison of the Results with Magneto-Optical Kerr Effect Measurements," *IEEE Trans. Magnetics* **16,** 375–378 (1980).
32. D. S. Lo, G. J. Cozimini, L. G. Zierhut, P. H. Dean, and M. C. Paul, "A Y-Domain Magnetic Thin Film Element," *IEEE Trans. Magnetics* **21,** 1776–1778 (1985).
33. A. Hubert, "Domain Wall Phenomena in Bubble Propagation Layers," *J. Magn. Magn. Mater.* **35,** 249–253 (1983).
34. B. W. Corb, "Effects of Magnetic History on the Domain Structure of Small NiFe Shapes," *J. Appl. Phys.* **63,** 2941–2943 (1988).
35. H. A. M. van den Berg and A. H J. van den Brandt, "Self-Consistent Domain Theory in Soft Ferromagnetic Media. III. Composite Structures in Thin-Film Objects," *J. Appl. Phys.* **62,** 1952–1959 (1987).
36. R. W. DeBlois, "Ferromagnetic and Structural Properties of Nearly Perfect Thin Nickel Platelets," *General Electric Report No. 65-C-083* (1962).
37. R. W. DeBlois, "Ferromagnetic Domain Studies in Highly Perfect Metal Platelets," *General Electric Report No. AFCRL-68-0414* (1968).
38. F. Smidt, W. Rave, and A. Hubert, "Enhancement of Magneto-Optical Domain Observation by Digital Image Processing," *IEEE Trans. Magnetics* **21,** 1596–1598 (1985).
39. R. W. DeBlois, "Ferromagnetic Domains in Single-Crystal Permalloy Platelets," *J. Appl. Phys.* **39,** 442–443 (1968).
40. S. R. Herd, K. Y. Ahn, and S. M. Kane, "Magnetization Reversal in Narrow Strips of NiFe Thin Films," *IEEE Trans. Magnetics* **15,** 1824–1826 (1979).
41. G. W. Garnett and W. D. Corner, "Domain Structure and Magnetization Process in Permalloy Propagation Elements," *J. Magn. Magn. Mater.* **30,** 11–26 (1982).
42. Y. Nakamura, K. Yamakawa, and S. Iwasaki, "Analysis of Domain Structure of Single Pole Perpendicular Head," *IEEE Trans. Magnetics* **21,** 1578–1580 (1985).
43. R. W. DeBlois and C. D. Graham, "Domain Observations on Iron Whiskers," *J. Appl. Phys.* **29,** 528–529 (1958).
44. R. W. DeBlois and C. D. Graham, "Domain Observations on Iron Whiskers," *J. Appl. Phys.* **29,** 931–939 (1959).
45. R. V. Coleman and G. G. Scott, "Magnetic Domain Patterns on Single-Crystal Iron Whiskers," *Phys. Rev.* **107,** 1276–1280 (1957).
46. R. V. Coleman and G. G. Scott, "Magnetic Domain Patterns on Iron Whiskers," *J. Appl. Phys.* **29,** 526–527 (1958).
47. G. G. Scott and R. V. Coleman, "Domain Changes During Longitudinal Magnetization of Iron Whiskers," *J. Appl. Phys.* **28,** 1512–1513 (1957).
48. L. Drewello and H. H. Mende, "Magnetic Domain Structures of Elastically and Plastically Deformed Iron Whiskers," *J. Magn. Magn. Mater.* **13,** 231–235 (1979).
49. F. A. N. van der Voort and H. A. M. van den Berg, "Irreversible Processes in Soft-Ferromagnetic Thin Films," *IEEE Trans. Magnetics* **23,** 250–258 (1987).
50. P. Molho, J. Gouzerh, J. C. S. Levy, and J. L. Porteseil, "Topological Hysteresis in Stripe Domain Structures," *J. Magn. Magn. Mater.* **54–57,** 857–858 (1986).
51. H. A. M. van den Berg and F. A. N. van der Voort, "Cluster Creation and Hysteresis in Soft-Ferromagnetic Thin-Film Objects," *IEEE Trans. Magnetics* **21,** 1936–1938 (1985).
52. R. P. Williams, "A Model of Magnetic Bubble Propagation Patterns Using Surface Charge Embedded in a Minimum Domain Configuration," *IEEE Trans. Magnetics* **17,** 2423–2433 (1981).
53. N. D. Merwin, "The Topological Theory of Defects in Ordered Media," *Rev. Mod. Phys.* **51,** 591–648 (1979).
54. G. Toulouse and M. Kléman, "Principles of a Classification of Defects in Ordered Media," *J. de Phys. (Paris)* **37,** L149–L151 (1976).
55. R. Vlaming and H. A. M. van den Berg, "A Theory of the Three-Dimensional Solenoidal Magnetization Configurations in Ferro and Ferri Magnetic Materials," *J. Appl. Phys.* **63,** 4330–4332 (1988).
56. H. A. M. van den Berg, "Corner Clusters in Thin Soft Magnetic Layers. I. Space-Charge-Density and Field Singularities," *J. Appl. Phys.* **54,** 3359–3369 (1983).
57. H. A. M. van den Berg and M. F. Dane, "Free Wall Clusters in Soft Ferromagnetic Layers," *J. Magn. Magn. Mater.* **27,** 71–84 (1982).
58. E. J. Hsieh and R. F. Soohoo, "Domain Boundary Configurations for Head-On Magnetization Patterns," *A. I. P. Conf. Proc.* **17,** 727–731 (1971).
59. M. Labrune, I. B. Puchalska, and A. Hubert, "Domain Propagation Along the Hard Axis in a One Fold Layer," *J. Magn. Magn. Mater.* **61,** 321–329 (1986).
60. R. H. Wade, "Investigations of the Geometrical-Optical Theory of Magnetic Structure Imaging in the Electron Microscope," *J. Appl. Phys.* **37,** 366–376 (1966).
61. R. W. Wade, "Contrast Effects at Edges and Cracks in Ferromagnetic Films Viewed by Electron Microscopy," *Brit. J. Appl. Phys.* **14,** 398–399 (1963).
62. S. R. Herd, K. Y. Ahn, and S. M. Kane, "Magnetization Reversal in Narrow Strips of NiFe Thin Films," *IEEE Trans. Magnetics* **15,** 1824–1826 (1979).
63. G. A. Jones, P. J. Grundy, and D. R. Brambley, "The Observation of Domain Structure in Bubble Propagation Circuits," *J. Phys. D* **11,** L165–L168 (1968).
64. P. J. Grundy and R. S. Tebble, "Lorentz Electron Microscopy," *Adv. Phys.* **17,** 153–242 (1969).
65. E. Feldtkeller and F. Fuchs, "Zur Wandstruktur in Dünnen Magnetischen Schichten," *Z. Angew. Phys.* **18,** 1–4 (1964).
66. H. A. M. van den Berg and D. K. Vatvani, "Wall Clusters in Thin Soft Ferromagnetic Configurations," *J. Appl. Phys.* **52,** 6830–6839 (1981).
67. Y. Gondo, B. E. Gran, and R. J. Prosen, "Lorentz Microscopic Examinations of Polycrystalline Films with Biaxial Properties," *J. Appl. Phys.* **36,** 1062–1063 (1965).
68. S. Middelhoek, in *Magnetic Properties of Materials,* J. Smit, Ed., McGraw-Hill Book Co., Inc., New York, 1972, p. 312.
69. A. Tonamura, "Observation of Magnetic Domain Structure in Thin Films by Electron Holography," *J. Magn. Magn. Mater.* **31–34,** 936–939 (1983).
70. A. Hubert, *Theorie der Domänenwände in Geordneten Medien,* Springer-Verlag, Berlin, 1974.
71. H. Riedel and A. Seeger, "Micromagnetic Treatment of Néel Walls," *Phys. Status Solidi* **46,** 377–383 (1971).
72. N. Smith, "A Specific Model for Domain-Wall Nucleation in Thin-Film Permalloy Microelements," *J. Appl. Phys.* **63,** 2932–2937 (1988).
73. E. Feldtkeller, "Übersicht über das Magnetisierungsverhalten in Dünnen Schichten," *Z. Angew. Phys.* **17,** 121–130 (1964).
74. H. Riedel, "Micromagnetic Theory of Large-Angle Ripples and Stripe Domains in Thin Ferromagnetic Films," *Phys. Status Solidi (A),* 449–460 (1974).
75. H. Hoffman, "Micromagnetism in Two Dimensions," *IEEE Trans. Magnetics* **15,** 1215–1218 (1979).
76. J. Nowak and E. Szibel, "Domain Splitting in Thin Films with In-Plane Anisotropy," *IEEE Trans. Magnetics* **20,** 2105–2109 (1984).

*Received November 1, 1988; accepted for publication March 28, 1989*

**Hugo A. M. van den Berg** *Zentral Forschungs Labor, Siemens A.G., Postfach 3240, Erlangen, Federal Republic of Germany.* Dr.

van den Berg received his M.S. degree from the Delft University of Technology at Delft, The Netherlands, in 1973. He remained as a staff member of the Laboratory for Electronic Materials at Delft, where his primary interests were the theoretical and experimental aspects of photolithography. Dr. van den Berg subsequently became interested in the magnetic domain configurations of soft-magnetic materials, and completed his Ph.D. dissertation on this subject in 1984. In 1987 he joined the staff of the Zentral Forschungs Labor of Siemens in Erlangen. Dr. van den Berg's main interests are currently the physics of magneto-optic and magnetic memories.